Tenascin-C orchestrates an immune suppressive tumor microenvironment in oral squamous cell carcinoma

Caroline Spenlé, Thomas Loustau, Devadarssen Murdamoothoo, William Erne, Stéphanie Beghelli-de La Forest Divonne, Romain Veber, Luciana Petti, Pierre Bourdely, Matthias Mörgelin, Eva Maria Brauchle, et al.

Tenascin-C orchestrates an immune suppressive tumor microenvironment in oral squamous cell carcinoma

Caroline Spenlé[1]*, Thomas Loustau[1]*, Devadarssen Murdamoothoo[1], William Erne[1], Stephanie Beghelli-de la Forest Divonne[2,3], Romain Veber[4], Luciana Petti[5], Pierre Bourdely[5], Matthias Mörgelin[6], Eva-Maria Brauchle[7,8,9], Gérard Cremel[1], Vony Randrianarisoa[1], Abdouramane Camara[4], Samah Rekima[2,3], Sebastian Schaub[2,3], Kelly Nouhen[5], Thomas Imhof[10], Uwe Hansen[11], Nicodème Paul[12], Raphael Carapito[12], Nicolas Pythoud[13], Aurélie Hirschler[13], Christine Carapito[13], Hélène Dumortier[4], Christopher G. Mueller[4], Manuel Koch[10], Katja Schenke-Layland[7,8,9], Shigeyuki Kon[14], Anne Sudaka[2,3], Fabienne Anjuère[5], Ellen Van Obberghen-Schilling[2+], Gertraud Orend[1+]

Running title: Immune suppressive microenvironment by tenascin-C

[1] Université Strasbourg, INSERM U1109- MN3T, The Microenvironmental Niche in Tumorigenesis and Targeted Therapy, and The Tumor Microenvironment Laboratory, Hopital Civil, Institut d'Hématologie et d'Immunologie, Fédération de Médecine Translationnelle de Strasbourg (FMTS), Strasbourg, France

[2] Université Côte d'Azur, CNRS, INSERM, iBV, France

[3] Centre Antoine Lacassagne, Nice 06189, France

[4] Institut de Biologie Moléculaire et Cellulaire, CNRS, UPR3572 Immunologie, Immunopathologie et Chimie Thérapeutique, Institut de Biologie Moléculaire et Cellulaire, Strasbourg

[5] Université Côte d'Azur, CNRS, IPMC, Valbonne-Sophia Antipolis, France

[6] Colzyx AB, Scheelevägen 2, 223 81 Lund, Sweden

[7] Dept. of Women's Health, Research Institute of Women's Health, Eberhard Karls University Tübingen, Silcherstr. 7/1, 72076 Tübingen, Germany

[8] The Natural and Medical Sciences Institute (NMI) at the University of Tübingen, Markwiesenstr. 55, 72770 Reutlingen, Germany

[9] Cluster of Excellence iFIT (EXC 2180) "Image-Guided and Functionally Instructed Tumor Therapies", Eberhard Karls University Tübingen, Germany

[10] Institute for Dental Research and Oral, Musculoskeletal Research, Center for Biochemistry, University of Cologne, 50931 Cologne, Germany

[11] Institute for Musculoskeletal Medicine (IMM), University Hospital Muenster, 48149 Muenster, Germany

[12] INSERM U1109, GENOMAX, 67091 Strasbourg

[13] IPHC, Cronenbourg

[14] Faculty of Pharmaceutical Sciences, Hokkaido University, Sapporo, Japan

* Equal contribution

+ Correspondence :

Ellen Van Obberghen-Schilling, Université Côte d'Azur, CNRS, INSERM, iBV, 06189 Nice, France, Ellen.VAN-OBBERGHEN@unice.fr

Gertraud Orend, INSERM U1109, The Tumor Microenvironment Laboratory, 67091 Strasbourg, France, gertraud.orend@inserm.fr, https://orend-tme-group.com

Abstract

Inherent immune suppression represents a major challenge in the treatment of human cancer. The extracellular matrix molecule tenascin-C promotes cancer by multiple mechanisms, yet the roles of tenascin-C in tumor immunity are incompletely understood. Using a 4NQO-induced oral squamous cell carcinoma (OSCC) model with abundant and absent tenascin-C, we demonstrated that tenascin-C enforced an immune suppressive lymphoid stroma via CCL21/CCR7 signaling, leading to increased metastatic tumors. Through TLR4, tenascin-C increased expression of CCR7 in CD11c+ myeloid cells. By inducing CCL21 in lymphatic endothelial cells via integrin $\alpha 9\beta 1$ and binding to CCL21, tenascin-C immobilized CD11c+ cells in the stroma. Inversion of the lymph node-to-tumor CCL21 gradient, recruitment of T regulatory cells, high expression of anti-inflammatory cytokines and matrisomal components were hallmarks of the tenascin-C-instructed lymphoid stroma. Ablation of tenascin-C or CCR7 blockade inhibited the lymphoid immune suppressive stromal properties, reducing tumor growth, progression and metastasis. Thus, targeting CCR7 could be relevant in human head and neck tumors as high tenascin-C expression and an immune suppressive stroma correlate to poor patient survival.

Introduction

Head and neck squamous cell carcinomas (HNSCC) are heterogeneous malignancies originating from the mucosal surface of the upper aero-digestive tract. The 5-year survival rate worldwide is around 50% due to disease recurrence and metastasis (1). At least two genetic subclasses of HNSCC can be distinguished, where Human Papilloma Virus (HPV)-negative tumors, representing approximately 65% of HNSCC are caused by chronic exposure to carcinogens including tobacco and alcohol (2). The first line treatment of HNSCC is surgery followed by radiotherapy and chemotherapy and recently immune checkpoint therapy where long-lasting effects are seen only in a fraction of patients (3-5).

HNSCC is an immune suppressive disease where the physiological microenvironment changes into a protumoral state accompanied by major changes in the extracellular matrix (ECM) (5–8). Tenascin-C (TNC) is one such ECM molecule, that impacts the progression of several tumor types through regulation of multiple cancer hallmarks (9–11). In a non-tumor context, TNC can serve as a danger associated molecular pattern (DAMP) molecule, and trigger more severe inflammation through integrin $\alpha 9\beta 1$ and TLR4 (12,13). Although TNC is mostly absent in normal tissues, TNC is expressed in reticular fibers of lymphoid tissues where it regulates leukocyte maturation (14,15). In cancer tissue (16–18) TNC is organized in tumor matrix tracks (TMT) that share certain features with reticular fibers and may play a role in immune cell functions in cancer tissue (10,11,14). Although TNC is one of the major ECM proteins upregulated in the matrix of HNSCC-associated fibroblasts (19), the precise roles of TNC in this disease have not yet been investigated.

To better understand how immune cells interact with the neoplastic stroma in HNSCC, here, we used the carcinogen 4-Nitroquinoline 1-oxide (4NQO)-driven murine model with abundant or absent TNC. 4NQO applied in the drinking water causes DNA adduct formation thus mimicking the effects of tobacco carcinogens and, induces malignant lesions mainly in the tongue and esophagus (20,21).

We identified TNC as a molecule involved in the immune suppressive TME in OSCC. Comparison of tumors in wildtype (WT) and TNC knockout (TNCKO) mice allowed us to

demonstrate a role for TNC in OSCC progression and lymph node invasion suggesting a mechanism by which the TNC-rich tumor matrix shaped an immune suppressive, protumoral microenvironment. These results provide relevant information for human HNSCC diagnosis and therapy.

Material and Methods

Human tumor samples and immunohistochemistry

Surgically removed tongue tumors, embedded in paraffin blocks, were retrieved from the archives of the Pathology Department of the Centre Antoine Lacassagne. Informed consent was obtained for all subjects. Patient characteristics are summarized in **Supplemental Table S1**. Hematoxylin and eosin staining and immunohistochemical methods were performed on serial 4 µm deparaffinized tissue micro array (TMA) sections. CD45 staining was performed on a BenchMark Ulter automated slide staining system (Ventana Medical Systems, Inc., Roche Group, Tuscon, AZ) using monoclonal anti-CD45 (LCA) (clone 2B11+PD7/26) or anti-podoplanin (D2-40) according to instructions of the manufacturer (Cell Marque, Rocklin, CA). For TNC staining, intrinsic peroxidase was blocked by incubating sections with 3% hydrogen peroxide for 15 minutes. Antigen retrieval was performed in EDTA buffer pH 9.0, in a de-cloaking chamber (Dako, catalog number S2367). Sections were blocked in 4 % goat serum for 1 hour, then incubated for 1 hour with mouse monoclonal anti-TNC (clone BC24, Sigma-Aldrich 1/1000). After rinsing with PBS, sections were incubated with biotinylated secondary antibody (30 minutes) and biotinylated goat anti-mouse IgG (30 minutes) followed by avidin-biotin (Vector Lab, VECTASTAIN ABC Kit, catalog number PK-4000). Slides were incubated with 3,3 ′-Diaminobenzidine developing solution (Vector Lab, DAB, catalog number SK-4100) and hematoxylin before embedding into ProLong Gold antifade reagent (Invitrogen, catalog number P36930). For fluorescence staining, after permeabilization (PBS, 0.1% Triton) cells/tissue were incubated with the primary antibodies (**Supplemental Table S2**) overnight. Bound antibodies were detected with the appropriate Alexa-labelled secondary antibodies (**Supplemental Table S2**) prior to nuclear staining with Dapi (Sigma,catalog number D9542) and embedding into ProLong Gold antifade reagent (Invitrogen, catalog number P36930). Fluorescently-stained sections were digitalized (40X) using a PerkinElmer Vectra Polaris imaging system and Phenochart software (Akoya Biosciences).

Quantification of human staining

Stained slides were scanned on the Hamamatsu NanoZoomer 2.0-HT Digital slide scanner (40X mode). Scans were viewed and images acquired using the NDP.view2 software. For quantification, we developed a script (based on ImageJ) optimized to be used with interactive surfaces (https://figshare.com/articles/Custom_toolbars_and_mini_applications_with_Action_Bar/3397603/3). The program and the manual are freely available at https://mycore.core-cloud.net/index.php/s/0K61LqHBrnNKShX. Randomly chosen images of non-invasive tumor areas (3 per tumor, 5X magnification) were projected on an interactive digital whiteboard. A pathologist determined the regions of interest (ROIs) corresponding to tumor cell nest or stroma. These ROIs where extracted after color deconvolution and thresholding to quantify CD45 staining. We then determined the ratio of area containing CD45 (holes were removed as deduced from the hematoxylin image) per image and per ROI type.

Patient survival and correlation matrix data

Public patient data (GSE27020) were analyzed by the Kaplan-Meier plotter tool (ProggeneV2 prognostic database) as described (22). The cohort was separated by the median of corresponding gene expression as “High” and “Low”, respectively. Gene expression was correlated to relapse free survival (RFS). The correlation matrix analysis by Corrplot package (R software) (https///github.com/taiyun/corrplot, Taiyn and Simko) was performed on gene expression data derived from RNA chip analysis from HNSCC tumors of 68 patients (23). The graphical representation was generated using the R package corrplot. The multiple testing corrections were performed using the pound method (24).

The 4NQO model and antibody treatment of tumor bearing mice

4-NQO (Sigma-Aldrich, catalog number N8141) was administered to 8 week old WT and TNCKO (KO) (26) mice, that had been bred in house with C57BL/6J mice (Charles River) for more than 10 generations, in the drinking water at a final concentration of 100 µg/ml for 16

weeks (stock 5 mg/ml in propylene glycol). Subsequently, mice were fed with regular water for 4 weeks before sacrifice, where tongue, submandibular lymph nodes, and spleen were collected and prepared for FACS analysis, cryosectioning, mRNA or protein extraction as described below. During tissue sampling, the general organ appearance and the number of tumors per 4 mice were determined. To assess the roles of CCL21/CCR7 signaling, mice were also subjected to the regular 4NQO protocol as described above. The last 2 weeks before sacrificing the mice, mice were given 3 intraperitoneal injections of IgG control antibody (200 µg, R&D systems, catalog number MAB006) or CCR7 antibody (200µg, R&D systems, MAB3477) as previously described (26). The injections were spaced at least 4 days apart and the last injection took place 4 days before the sacrifice. All mice were housed and handled according to the guidelines of INSERM and the ethical committee of Alsace, France (Cremeas; Directive 2010/63/EU on the protections of animals used for scientific purposes).

Gene expression analysis

RNA from WT and TNCKO tongue tumors (3 samples per group) was isolated using the RNeasy Mini Kit (Qiagen, catalog number 74104) and RNA integrity was determined with an Agilent Bioanalyzer 2100 (Pico Kit, Agilent Technologies). Total RNA Sequencing libraries were prepared with SMARTer Stranded Total RNA-Seq Kit v2 - Pico Input Mammalian (TaKaRa, catalog number 634411) according to the manufacturer's protocol. Libraries were pooled and sequenced (paired-end 2*75bp) on a NextSeq500 using the NextSeq 500/550 High Output Kit v2 according to the manufacturer's instructions (Illumina, catalog number 20024907). Quality control of every sample was assessed with the NGS Core Tools FastQC and sequence reads were mapped using STAR and Bowtie2 (27,28). The total mapped reads were finally available in BAM (Binary Alignment Map) format for raw read counts extraction. Read counts were found by the HTseq-count tool of the Python package HTSeq (29) with default parameters to generate an abundance matrix. Differential analyses were performed using the DESEQ2 (30) package of the Bioconductor framework. Up-regulated and down-regulated genes were selected based on the adjusted p-value (<0.10) and the

fold-change (> +/- 0.8) (**Supplemental Table S3)**. Deregulated gene expression analysis was performed by using the PANTHER version 11 (31) and REACTOME software (32).

Nano-LC-MS/MS analysis

Tongue tumor pieces from WT and TNCKO mice were resuspended in Laemmli buffer (10 mM Tris pH 6.8, 1mM EDTA, 5% ß-mercaptoethanol, 5% SDS, 10 glycerol, 1/100 antiproteases). Proteins were extracted for 1 hour upon sonication (4 times for 5 minutes). Protein concentration was determined using the RC-DC protein assay (Bio-Rad, catalog number 5000121) following the manufacturer's instructions. Forty µg of protein lysate for each sample were heated at 95°C for 5 minutes and stacked in an in-house prepared 5% polyacrylamide SDS-PAGE stacking gel. Gel bands were reduced and alkylated prior to overnight digestion (the ratio of enzyme/protein = 1/50) at 37°C using modified porcine trypsin (Promega, catalog number V5113). The generated peptides were extracted with 60% acetonitrile (ACN) in 0.1% formic acid (FA) followed by a second extraction with 100% ACN. Peptides were resuspended in 100 µL of water and 0.1% formic acid.

Nano-LC-MS/MS analysis was performed on a nanoAcquity UPLC devise (Waters) coupled to a Q-Exactive HF-X mass spectrometer (Thermo Scientific) equipped with a Nanospray Flex ion source. Peptide separation was performed on an ACQUITY UPLC Peptide BEH C18 Column (250 mm x 75 µm with 1.7 µm diameter particles) and an ACQUITY UPLC M-Class Symmetry C18 Trap Column (20 mm x 180 µm with 5 µm diameter particles; Waters). The solvent system consisted of 0.1% FA in water (solvent A) and 0.1% FA in ACN (solvent B). Samples (800 ng) were loaded into the enrichment column over 3 minutes at 5 µL/min with 99% of solvent A and 1% of solvent B. Peptides were eluted at 400 nL/min with the following gradient of solvent B: from 1 to 8% over 2 minutes, from 8 to 35% over 77 minutes, and from 35 to 90% over 1 minute. Samples were injected in a randomized order. The MS capillary voltage was set to 2 kV at 250°C. The system was operated in a data-dependent acquisition mode with automatic switching between MS (mass range 375-1500 m/z with R = 120 000 at 200 m/z, automatic gain control fixed at 3 x 106 ions, and a maximum injection time set at 60 milliseconds) and MS/MS (mass range 200-2000 m/z with R = 15 000 at 200 m/z, automatic gain control fixed at 1 x 105, and the maximal injection time set to 60 milliseconds) modes. The twenty most abundant peptides were selected on each MS spectrum for further isolation and higher energy collision dissociation (normalized collision energy set to 27), excluding

unassigned, monocharged and superior to seven times charged ions. The dynamic exclusion time was set to 40 seconds, and “Peptide match selection” parameter of the software.

The raw data obtained for each condition were processed with MaxQuant (version 1.6.0.16) (33). Peaks were assigned with the Andromeda search engine with full trypsin (Trypsin/P) specificity against an in-house generated protein sequence database containing all mouse protein entries extracted from UniProtKB-SwissProt (17 007 sequences, taxonomy identifier: 10 090, release 2019-04-09). Carbamidomethylation of cysteines was set as fixed modification whereas oxidation of methionines and protein N-terminal acetylation were defined as variable modifications. Minimal peptide length was set to seven amino acids and up to two missed cleavage sites were allowed for trypsin digestion. Peptide mass tolerance was set to 20 ppm for the first search and 5 ppm for the main search. The maximum false discovery rate was 1% at PSM, peptide and protein levels with the use of a target/decoy strategy.

Label-free quantification was done on unique peptides (LFQ min. ratio count of 2) with the match between runs option activated (match window of 2 min and alignment window of 10 minutes). Unmodified peptides and those with carbamidomethylated cysteines were used for protein quantification.

After removal of contaminants, reverse entries, proteins only identified with modified peptides and protein groups identified with less than two unique peptides, differential analyses on normalized LFQ intensities were performed using Prostar (version 1.16.6) (34). A Limma t-test was performed for the statistical analysis test calibrated with the pounds method (35). Dysregulated proteins were selected based on the adjusted p-value (**Supplemental Table S4**) and further analysis were performed using the PANTHER version 11 (31) and REACTOME software (32).

Proteome profiler array

Proteins were extracted from 5 WT, 5 KO, 4 Control Ab and 4 CCR7 Ab tongue tumors in lysis buffer (Triton 1X and protease inhibitors (Roche, catalog number 11697498001) diluted

in 1X PBS) following the manufacturer's instructions and protein concentration of tumor samples was determined by optical density measurement (NanoDrop 2000). The expression of immunomodulatory molecules in tumor samples was measured using the Mouse XL Cytokine Array Kit (Biotechne, catalog number ARY028) according to the manufacturer's instruction. After membrane blocking, equal protein amounts from 4 or 5 pooled tumors per group were applied to the membrane overnight. Two membranes were used for each group to have an experimental duplicate. The revelation of each membrane was done by using the Cemi Reagent Mix provided in the kit and a Chemidoc Imager XRS (BioRad). Quantification was done by measuring pixel density with the Image J software. The background signal was subtracted with the negative control spots and the positive control spots were used to normalize values of each molecule in order to compare membranes between each other (**Supplemental Table S5)**.

Hematoxylin-Eosin staining (HE)

The OCT embedded tissue sections (8µm thick) were incubated in ddH_20 before staining with hematoxylin (Surgipath, catalog number 3801560) for 30 secondes and eosin (Sigma, catalog number HT110132) for 10 secondes, spaced by 1 minute of dd H_20 washes. After the last wash, tissue sections were dehydrated 5 minutes in increasing percentage baths of ethanol (from 70 to 100%) and toluene and then covered with the Eukitt solution (Sigma, catalog number 03989).

Immunofluorescence

For IF staining, unfixed frozen sections of 8 µm or cells fixed with 4% paraformaldehyde were incubated for 1 hour at room temperature with blocking serum (5% normal goat or donkey serum in PBS; Jackson ImmunoResearch, catalog number 005-000-121 and 017-000-121, respectively)

and overnight directly with the primary antibodies (**Supplemental Table S5**). Bound antibodies were visualized with goat, rabbit, guinea pig, hamster, or rat secondary antibodies

conjugated with Alexa 488, Cy3 or Cy5. Dapi (Sigma) was used to visualize nuclei. After embedding in FluorSave Reagent (Calbiochem, catalog number 345789), sections were examined using a Zeiss Axio Imager Z2 microscope. Pictures were taken with an AxioCam MRm (Zeiss,) camera and Axiovision software. Control sections were processed as mentioned above with omission of the primary antibodies. The image acquisition setting (microscope, magnification, light intensity, exposure time) was kept constant per experiment and in between experimental conditions. For quantification of immune cells and positive staining area, the ImageJ software was used. CCL21, CCR7 and gp38 scoring is based on the criteria described in **Supplemental Table S6**. At least 2 sections of 5 different tumors/mice were quantified per condition. The number of immune cells was reported in correlation to the total number of Dapi positive cells.

Electron microscopy

Frozen and cryopreserved tissue samples were thawed and washed for 15 minutes with distilled water followed by a fixation in 2% (v/v) formaldehyde and 0.25% (v/v) glutaraldehyde in 100 mM cacodylate buffer, pH 7.4, at 4°C overnight. Afterwards, tissue samples were rinsed in PBS, dehydrated in ethanol up to 70% (each step 30 minutes), and embedded in LR White embedding medium (London Resin Company, UK, catalog number 14381-UC) using UV light for polymerization (Leica EM AFS). Ultrathin sections were cut with an ultramicrotome (Leica Ultracut UCT), collected on copper grids (Athene Grids, G202) and negatively stained with 2% uranyl acetate (Serva, catalog number 77970) for 15 minutes. Electron micrographs were taken at 60 kV with a Phillips EM-410 electron microscope using imaging plates (Ditabis, Pforzheim, Germany).

Raman microspectroscopy

Raman images were acquired using a WITec alpha300R Raman microscope (WITec, Ulm Germany). In the upright set-up a 532 nm laser was focused through a 60x dipping objective (NA 1.0) to excite Raman scattering on tissues sections. Tissue areas within the TMTs of

150 x 200 µm were scanned using a pixel size of 1 µm and an acquisition time of 0.08 seconds per pixel. For each tumor 2-3 Raman images were generated. The spectral images were then further processed and analyzed using WITec Project Five software (WITec, Ulm, Germany). After cosmic ray removal and background correction, spectra of each pixel were area-normalized. The tumor stroma was identified based on a specific spectral pattern, predominantly resembling collagen fibers. For each image all pixels resembling this matrix pattern were averaged. Spectral patterns of stromal matrix in WT and TNCKO were compared using univariate statistics and (Principal Component Analysis) PCA. To identify CCL21 in the tumor stroma, a reference spectrum of purified mouse CCL21 (457-6C; R&D systems) was acquired. Peaks at 757,1030, 1210, 1319 and 1615 cm^{-1} are specific for CCL21. This spectrum was used to decompose the ECM spectra in a True Component Analysis (WITec). Here the CCL21 reference was first employed on a CCL21-positive lymph node to identify CCL21 in a physiological condition. The CCL21 spectrum was extracted from the lymph node Raman scans and employed on the Raman data from tumor stroma. For quantification relative intensities of CCL21 in WT and TNCKO stroma was normalized to the collagenous stroma area.

TNC cloning and purification

Recombinant his-tagged human TNC was purified as described (36,37). and used for incubation with cells. Murine strep-tagged TNC was used in negative EM microscopy and treatment of cells. For cloning murine TNC, a PCEP4 expression vector (Invitrogen, catalog number V04450) with TNC (NP_035737.2, aa: 174-2019) from Mus musculus has been obtained from R. Chiquet-Ehrismann (FMI, Basel, Switzerland). The coding sequence was modified with a BM40 signal peptide and a N terminal double strep II tag and was confirmed by sequencing (**Supplemental Table S7)**. In order to generate stable cell lines, HEK293 EBNA cells were transfected with the expression vector using Fugene HD (Promega, catalog number E2311). After 48 hours of transfection, the medium was replaced with 0.5 µg/ml containing DMEM/F12 medium with 10% FCS and the cells were grown to confluency. The protein was then purified from the supernatant by using the Streptactin matrix (IBA, Lifesciences, catalog number 2-1021-001) following the manufacturer's guidelines and was then dialyzed 3 times against PBS as previously described (37).

Surface plasmon resonance spectroscopy

Surface plasmon resonance binding experiments were performed on a Biacore 2000 instrument (Biacore Inc.) at 25°C. Recombinant human TNC (36) was immobilized at high surface density (around 7000 resonance units) on an activated CM5 chip (Biacore Inc., catalog number 29149604) using a standard amine-coupling procedure according to the manufacturer's instruction. Soluble molecules were added at a concentration of 10 µg/ml in 10 mM sodium acetate, pH 5.0, and at a flow rate of 5 µl/minute for 20 minutes before addition of 1 M ethanolamine. CCL21 (0.5, 0.87 and 2µg in 200µl) was added to the chip at pH 6.0 (10 mM MES, pH 6.0, 150 mm sodium chloride, 0.005% (v/v) surfactant P20), or at pH 7.4 (10mM HEPES, 150 mM sodium chloride, 0.005% (v/v) surfactant P20), at a flow rate of 10 µl/minute. A blank CM5 chip was used for background correction. 10 mM glycine, pH 2.0, at 100 µl/minute for one minute was used to regenerate the chip surface between two binding experiments. A steady state condition was used to determine the affinity of CCL21

for TNC. The Dissociation constant (Kd) was determined using the 1:1 Langmuir association model as described by the manufacturer (https://www.biacore.com/lifesciences/help/kinetic_model_1_1_binding/index.html).

Negative staining, transmission electron microscopy and CCL21 binding assay

The interaction of TNC with CCL21 was visualized by negative staining and transmission electron microscopy as described previously (38). Briefly, TNC samples (20 nM) were incubated with a 3 molar excess of CCL21 (457-6C-025 R&D systems) for one hour at 37°C in tris buffered saline (TBS), pH 7.4. For visualization in the electron microscope CC21 was conjugated with 5 nm colloidal gold (39). For inhibition experiments, TNC samples were pre-incubated with a 10 molar excess of heparin for one hour at 37°C. Specimens were examined in a Philips/FEI CM 100 TWIN transmission electron microscope operated at 60 kV accelerating voltage. Images were recorded with a side-mounted Olympus Veleta camera with a resolution of 2048 x 2048 pixels (2k x 2K) and the ITEM acquisitions software. Binding of CCL21 particles to TNC was determined by counting the number of gold particles along the length of the TNC monomer. Number of molecules from 500 randomly picked distinct TNC molecules were determined. As positive control, TGFβ1 was used as it binds in the 5th FNIII repeat of TNC (40). As negative controls EGF (shown not to bind to TNC (40)) and BSA were used, respectively.

Cell culture

All cultured cells were checked for the absence of mycoplasms (once every two months, PlasmoTest, Invivogen catalog number rep-pt1). LEC and DC-like DC2.4 were purchased from ATCC (HDMVECn, PCS-110-010, 2018) and Merck (SCC142, 2018), respectively and re-authenticated by determination of LYVE-1 expression (LEC), CD31 (HDMVEC) and CCR7, CD80 and CD86 (DC2.4) by flow cytometry. DC2.4 cells were cultured in DMEM-glucose (Dutscher) complemented with 10% of fetal bovine serum (FBS, Dutscher), 100 U/mL penicillin, 100 µg/mL streptomycin (PenStrep, Dutscher), 40 U/mL Gentamicin

(ThermoFisher Scientific) and 1X Hepes. LECs were cultured in ECGM with PenStrep, gentamicin and a supplemental growth factor cocktail according to Promocell (catalog number C22110). FRCs (Fibroblastic Reticular Cells) were isolated from the lymph nodes (popliteal, inguinal, brachial, axillary, mandibular and cervical) of a naïve WT mouse (10 weeks old) as described previously (41). FRCs were cultured in DMEM-glucose complemented with 10% FBS, 1% penstrep (Sigma catalog number P4333) and gentamicin (Dutscher catalog number P06-03100). The OSCC13 cell line was established from a primary 4NQO-induced tongue tumor of a WT mouse. Cells were mechanically dissociated and cultured in DMEM-F12 with 4.5g/L glucose, 10% FBS, 1% penstrep (Sigma catalog number P4333), gentamycin and 0.4µg/mL hydrocortisone (Sigma, catalog number H4001). Cells were cultured for 20 passages and then subcutaneously grafted in the neck of a WT mouse. After 2 times of grafting in WT C57Bl6-J mice, cells were cultured for 50 passages before use. Silencing of TNC in OSCC13 cells was done by short hairpin (sh) mediated gene expression knockdown. Briefly, lentiviral particles shRNA vectors (Sigma, catalog number SHCLNV-NM_011607 MISSION shRNA Lentiviral Transduction Particles) encoding specific shRNAs for the knock-down of TNC were used (shTNC:CCGGGCATCAA-CACAACCAGTCTAACTCGAGTTAGACTGGTTGTGTTGATGCTTTTTG). Lentiviral particles encoding a non-targeting shRNA vector were used as control (SHC202V, Sigma). Transduced cells were selected with the previously described DMEM-F12 culture medium supplemented with 10 µg/mL puromycin (Thermofisher, catalog number A1113802) and the selection pressure was kept in all in vitro experiments.

All cell lines were maintained at 37°C in a humidified atmosphere of 5% CO_2. The culture medium was refreshed every 2-3 days and passaged into a new dish with trypsin-EDTA (PanBiotech) upon reaching confluency. Cells were starved with DMEM-F12 medium containing 1% FBS overnight before treatment. Cells were treated for 24 hours with purified human or mouse TNC (10 µg/ml) diluted with DMEM medium complemented with 1% FBS, penstrep and gentamicin. Upon TNC stimulation, the conditioned medium (CM) was collected, filtered at 0.22 µm and stored at -80°C for future use. Cells were detached

mechanically, concentrated by centrifugation and lysed in Trizol reagent (Invitrogen, catalog number 12044977) before storage at -80°C. Before TNC incubation, LEC were pretreated with inhibitors for TGFβRI (GW788388, 10μM, 45 minutes, Selleckchem, catalog number S2750), TLR4 (Cli95, 1μg/mL, 6 hours, InvivoGen, catalog number tlrl-cli95), receptor tyrosine kinases (SU6668, 30μM, 60 minutes, Tocris bioscience, catalog number 3335), integrin α1β9 (blocking antibody α9Ab, 4μg/mL, 6 hours, provided by Shigeyuki Kon (20) and α9β1/α4β1, BOP, 1μM, 45 minutes, Tocris bioscience, catalog number 6047).

DC2.4 activation assay

DC2.4 were starved with medium containing 1% FBS overnight and pretreated the day after with TLR4 (Cli95, 1μg/mL, 6 hours) diluted in 1% FBS complemented DMEM-medium. Cells were incubated for 24 hours with 1% FBS complemented DMEM-medium containing lysophosphatidic acid (LPS) (1μg/mL) or soluble TNC (10μg/mL). Upon LPS or TNC incubation cells were detached, lysed in Trizol (Invitrogen) following the manufacturer's instructions or stained with anti-CD80-FITC, anti-CD11c-PE, anti-MHCII-APC EF780 and anti-CD86-PE Cy7 from eBiosciences for FACS analysis.

Boyden chamber migration assay

Boyden chamber migration assays on DC2.4 were performed in 5 μm-pore sized polycarbonate membrane transwells (Corning Costar Co, catalog number 3421). The lower surface of the transwells were pre-coated with Col I (BD biosciences, catalog number 354236), horse purified fibronectin (FN) (36) and mouse purified TNC at a final concentration of 1 μg/cm², respectively. The lower chambers of the transwells were filed with DMEM-medium containing mouse or human CCL21 (100 ng/mL, 200 ng/ml or 400 ng/ml, R&D systems, catalog number 457-6C-025 and 366-6C-025). To assess the migration of DC2.4 towards the secretome of the LECs, conditioning medium (CM) from LECs (treated or not with TNC (10μg/ml) for 24 hours) was placed in the lower chamber. In order to block the chemotaxis of DC2.4 cells towards CCL21, cells were incubated 6 hours with a CCR7

neutralizing antibodies (10µg/mL, R&D systems) diluted in 1% FBS complemented DMEM-medium. DC2.4 (5.1^5) suspended in 150 µl of 1% FBS complemented DMEM-medium were placed into the upper chamber of the transwell system. Cells were incubated for 5 hours (CCL21 in the lower chamber) or 8 hours (CM in the lower chamber) at 37°C in 5% CO^2. The number of migrated cells in the lower chamber was assessed by flow cytometry after the staining of DC2.4 with anti-CD11-PE (eBiosciences).

Boyden chamber chemoretention assay

The DC2.4 chemoretention assays were done with the same set up as described in the migration protocol. After 5 hours (CCL21 conditions) or 8 hours (CM conditions) of migration, the DC2.4 cells attached to the lower surface of the transwells were fixed in 4% PFA and stained with Dapi. Pictures were taken and analyzed by the ImageJ software.

RNA extraction and real-time quantitative PCR (qRTPCR)

Frozen tongue tumors and cultured cells were dissolved in the TRizol reagent (Invitrogen, catalog number 12044977) for total RNA extraction. RNA quality was confirmed by optical density measurement (OD 260 nm). cDNAs were synthesized from 1000 µg of total RNA using random primers and Moloney murine leukemia virus reverse transcriptase (MultiScribe, Applied Biosystems, catalog number 10117254). The cDNA was used for qRTPCR in an Mx3005P Real-Time PCR System (ThermoFisher Scientific). Reactions were carried out in duplicate for all conditions using a Sybr Green Master mix (ThermoFisher Scientific, catalog number 4344463) or Fast Taqman mix (ThermoFisher Scientific, catalog number 4444557) and expression of mouse or human *Gapdh* mRNA (Life Technology, catalog number 433764T) was used as endogenous control in the comparative cycle threshold method ($2^{-\Delta\Delta Ct}$). Primer sequences used for qPCR determination are listed in **Supplemental Table S8**.

Analysis of protein expression

Tissues or cell lysates were prepared in lysis buffer (50mM TRis-HCl ph 7.6, 150mM NaCl, 1% NP-40, 0.5% sodium deoxycholate and 0.1% SDS) supplemented with a phosphatase inhibitor cocktail (Santa Cruz, catalog number sc-45045) and protease inhibitors (Roche, catalog number 05892970001). The protein concentration of tissue samples and conditioned medium was determined by Bradford assay (BioRad, catalog number 5000001) following manufaturer's instructions. Thirty µg of protein lysate was loaded in precasted 4-20 % gradient gels (BioRad, catalog number 4561096), together with Laemmli buffer (BioRad, catalog number 1610737)

and separated by SDS-PAGE. The separated proteins were then transferred onto nitrocellulose membranes (BioRad**,** catalog number 1620113) using the TransBlot Turbo Transfer system (Biorad). Nitrocellulose membranes were then blocked with 5 % Blocking-Grade blocker (Biorad, catalog number 1706404) in 0.1% Tween-20 PBS and incubated with the primary antibody (overnight at 4°C) and secondary antibodies (one hour at room temperature) in 1.5 % Blocking-Grade Blocker in 0.1 %Tween-20 PBS. Antibodies used are listed in **Supplemental Table S2**. Protein bands were detected with the Amersham ECL Western Blotting detection reagent (GE Healthcare, catalog number RPN2106) or SuperSignal West Femto Maximum Sensitivity Substrate (ThermoFisher, catalog number 34095). CCL21 and IFNγ expressions were determined by using the 6-Ckine ELISA kit (ThermoFisher Scientific, catalog number EMCCL21A) and IFNγ ELISA kit (ThermoFisher Scientific, catalog number BMS606), respectively according to the manufacturer's instructions. The absorbance of each sample and standard was measured with a plate reader (MultiSkan EX, Thermo).

Flow cytometry

Tongue tumors and submandibular lymph nodes were cut into small pieces and inflated with digestion solution containing 1 mg/mL Collagenase D (Roche, catalog number 50-100-3282) and 0.2 mg/mL DNase I (Roche catalog number 4716728001), 2% inactivated fetal bovine serum in RPMI, at 37°C for 2 hours. Upon completion of digestion, 92 µL of 54 mM EDTA

Author Manuscript Published OnlineFirst on July 14, 2020; DOI: 10.1158/2326-6066.CIR-20-0074
Author manuscripts have been peer reviewed and accepted for publication but have not yet been edited.

was added and the samples were vortexed at maximal speed for 30 seconds. The resulting cell suspensions were passed through a 70 µm and 40 µm cell strainer and treated with flow cytometry buffer (PBS, 2% FBS, 1mM EDTA). After cells were counted, 2 x 10^6 cells per lymph node/spleen sample or 1 x 10^6 cells for tumor sample, were stained with Dead viability dye-efluor 450 (Thermo Fisher, catalog number 65-0863-18) according the manufacturer's instructions. Cells were then incubated in blocking solution containing 2% FcBlock CD16/CD32 (Thermo Fisher, catalog number 14-0161-85) in flow cytometry buffer, for 15 minutes at 4°C and then stained 30 minutes at 4°C with a standard panel of immunophenotyping antibodies; solution 1: anti-CD45-FITC, anti-CD11c-PE, anti-B220-APC, anti-MHCII-APC EF780 and anti-CCR7-Percp Cy5; solution 2: anti-CD45-FITC, anti-CD3e-PE, anti-C8a-APC, anti-CD4-APC EF780, anti-Foxp3-PE Cy7, anti-CCR7-Percp Cy5 and anti-CD25-AF700; solution 3: anti-CD45-FITC, anti-Gp38-PE, anti-CD31-APC, anti-F4/80-APC EF780, anti-CCR7-Percp Cy5 and anti-CD11b-AF700 (**Supplemental Table S2**). Data were acquired with a Beckman Coulter Gallios flow cytometer. Adjustments and data analysis were performed by using the FlowJo software. See **Supplemental Table S2** for information on the antibodies and **Supplemental Table S9 – S16** for information on the gating strategy.

Statistical analysis

For all data, Gaussian distribution was tested by the d'Agostino-Pearson normality test. When data followed a Gaussian distribution, statistical differences were analyzed by unpaired t-test (with Welch's correction in case of unequal variance) or ANOVA one-way with Tukey post-test. Otherwise, the Mann Whitney test or a non-parametric ANOVA followed by Dunns post-test were used to verify significance of the observed differences. All statistical analyses were performed using the GraphPad Prism software. Mean ± SEM. p values < 0.05 were considered as statistically significant, *p < 0.05; **p < 0.01; ***p < 0.001.

Results

TIL were enriched in the tenascin-C-rich stroma of OSCC

In contrast to non-tumoral human tongue tissue, with weak TNC expression, TNC expression was upregulated in the tongue tumor stroma, in TMT (17,18) (**Fig. 1A**). Investigating abundance of TIL (CD45+ leukocytes) revealed more TIL in the tumor stroma compared to the tumor nests **(Fig. 1B, C, S1B, C)**.

Tenascin-C enhanced OSCC onset and progression in 4NQO-induced OSCC

4NQO induced OSCC in the mucosal epithelium of mice **(Fig. 1D, S1D, E)** which recapitulated human OSCC **(Supplemental Fig. S1F)**. Whereas TNC expression was very low in tongue epithelium of non-treated mice, its expression became upregulated in the stroma of the OSCC **(Fig. 1E)**.

To address whether TNC had an impact on tumorigenesis in this model we determined tumor formation in WT and TNCKO mice. TNCKO mice presented a reduced number of tumors per mouse in comparison to WT mice **(Fig. 1F)**. Without TNC, tongue tumors were also significantly smaller than in WT mice **(Fig. 1G)**. TNCKO mice did not develop invasive carcinomas, in contrast to WT mice **(Fig. 1H)**. WT mice developed lymph node metastasis (p63 staining), which was absent in TNCKO mice (**Fig. 1I, J**).

Tenascin-C impacted the composition and organization of the stromal niches

Malignant tumor cells retained their epithelial (E-cadherin+, CK8/18+ and vimentin-negative) traits (**Supplemental Fig. S2A**). Tumor epithelial cell nests (p63+) were separated by stromal niches (αSMA+ cells), similar to human OSCC (**Supplemental Fig. S2A,** (42)). Tumors were highly vascularized (CD31 and LYVE-1) similar to human OSCC (43). No difference in vascularization, nor survival or proliferation was seen between tumor genotypes unlike other tumors (**Supplemental Fig. S2B-G**), (5,16,44).

Several genes (176) were differentially expressed, 120 up- and 56 down-regulated in WT compared to the TNCKO tumors (**Supplemental Table S2**). Expression of matrisome genes (45) was largely reduced in TNCKO tumors **(Supplemental Fig. S2H, S2K, Supplemental Table S3).** The analysis of the matrix by Raman microspectroscopy revealed a significant difference in the PC1 (Principal component) score that was below (TNCKO tumors) and above zero (WT tumors) (**Fig. 2A, B, S2 I, J**). TNC expression was not detected in the TNCKO tumors (**Fig. 2C**). Collagen networks differed in WT and TNCKO mice, with more parallel oriented and compactly organized collagen fibrils, in WT tumors (**Supplemental Fig. S2L**). TNC was expressed in TMT together with laminin (LM), fibronectin (FN), Coll IV and Coll XII **(Fig. 2C, S2M, N**).

Tenascin-C promoted leukocyte enrichment in the stroma

There was no difference in the abundance of CD45+ leukocytes between the two genotypes (**Fig. 2D**). However, there were more TIL in the tumor cell nests of TNCKO tumors (**Fig. 2E, F**). Whereas no difference in the abundance of macrophages (F4/80+, CD11b+), B cells (B220+), CD4 (CD3+, CD4+) or CD8 T lymphocytes (CD3+, CD8+) between tumor genotypes was seen we observed more dendritic cells (DC) (MHCII+/CD11c+) in TNCKO tumors (**Fig. 2G, Supplemental Fig. S2O**). CD11c+ cells resided predominantly in the stroma of WT tumors whereas more CD11c+ cells infiltrated tumor cell nests in TNCKO tumors (**Fig. 2H, I**). In contrast to DCs, Tregs (CD4+/Foxp3+) were more abundant inside the tumor cell nests of WT tumors (**Fig. 2J-L**). Macrophages (F4/80, CD206), CD4+ and CD8+ T lymphocytes, and B cells (B220) were present inside the tumor cell nests and the stroma with no apparent differences between WT and TNCKO tumors (**Supplemental Fig. S2R**). Thus TNC appears to orchestrate the intratumoral distribution of some leukocytes, in particular CD11c+ cells and Treg.

As CD11c+ cells are antigen presenting cells (APCs) that play a role in priming T cells in the lymph nodes (46), we investigated the immune cell infiltrate of the local lymph nodes by flow cytometry. We observed more CD45+ leukocytes in lymph nodes from TNCKO tumor mice

(**Supplemental Fig. S2P**). Whereas the abundance of macrophages, B cells and CD8 T cells was similar between genotypes, CD11c+ DC and CD4 T cells were more frequent in lymph nodes from the TNCKO mice (**Supplemental Fig. S2Q**). Less CD11c+ cells in the lymph nodes and a reduced lymph node-to-tumor ratio of these cells in WT (251-fold) compared to TNCKO mice (878-fold) indicated that TNC may have impaired the migration of CD11c+ cells towards the draining lymph nodes **(Fig. 2D, S3P)**. A higher proportion of lingual-derived DC (high expression of MHCII and intermediate expression of CD11c) (47), was observed in TNCKO lymph nodes compared to WT tumor mice indicating that DC homing to lymph nodes was reduced in WT conditions (**Supplemental Fig. S2S, T**).

Tenascin-C induced CCL21 in lymphatic endothelial cells

We observed increased CCL21 (+74%) and CCL19 (+17%) expression in WT tumors (**Fig. 3A, Supplemental Table S4**). We confirmed higher *Ccl21* mRNA and CCL21 protein expression in WT tumors (**Fig. 3B, C, Supplemental Table S6**). We also determined CCL21 expression in local lymph nodes and observed lower expression in lymph nodes compared to the tumors in WT mice, which could impact DC attraction to the lymph nodes (**Fig. 3C**). We observed no obvious difference in CCL21 and CD11c+ cell abundance and localization within the lymph nodes of WT and TNCKO tumor mice (**Supplemental Fig. S3A**).

We used Raman microspectroscopy across the whole tumor. Based on specific signals of the purified CCL21 protein, we detected a similar spectrum for CCL21 in Raman images of lymph nodes and, in WT and TNCKO tumors. Despite a strong background due to collagen-rich matrix, CCL21 specific peaks were identified in lymph nodes (a known source of CCL21) and stroma of WT and TNCKO tumors, whereas they were absent from the tumor cell nests, and lung tissue (**Fig. 3D, E, S3B**). CCL21 was significantly lower in TNCKO compared to WT tumors (**Fig. 3F-H**). Lymphatic endothelial cells (LEC), typically expressing LYVE-1 and CCL21, expressed CCL21 in the OSCC which was much less pronounced in TNCKO tumors (**Fig. 3I**). Reduced CCL21 expression was not due to less LEC in TNCKO tumors, as LEC were similarly abundant in TNCKO as in WT tumors (**Supplemental Fig. S2B–F**). Staining

Author Manuscript Published OnlineFirst on July 14, 2020; DOI: 10.1158/2326-6066.CIR-20-0074
Author manuscripts have been peer reviewed and accepted for publication but have not yet been edited.

for CCL19, the second ligand for CCR7 revealed similar staining intensity and stromal localization in the tumors and no difference in lymph nodes of WT and TNCKO mice (**Supplemental Fig. S3C, D)**.

We examined whether TNC induced CCL21 in LEC and fibroblastic reticular-like cells (FRC), which reside in tumors (48) and naturally express CCL21 (49). We used human dermal LEC expressing LYVE-1, gp38 and integrin $\alpha 9\beta 1$ (**Supplemental Fig. S3E**) and isolated FRC (typically expressing ERTR7 and gp38, (41)) from lymph nodes of a naïve WT mouse (**Supplemental Fig. S3F**). Upon exposure to TNC there was no difference in FRC and OSCC13 (isolated from a 4NQO-induced carcinoma, typically expressing p63 and CK8/18 (50) (**Fig. 3J, Supplemental Fig. S3F, G)**. However, *Ccl21* mRNA and CCL21 protein expression largely increased in LEC upon treatment with TNC (**Fig. 3K, Supplemental Fig. S3H**).

Inhibitors for TGFβRI (GW788388), TLR4 (Cli95) and receptor tyrosine kinases (SU6668) did not alter CCL21 expression upon TNC treatment, but an antagonist for integrins $\alpha 4\beta 1/\alpha 9\beta 1$ (BOP) and an integrin $\alpha 9\beta 1$ blocking antibody reduced *Ccl21* mRNA and CCL21 protein expression compared to those without induction by TNC (**Fig. 3K, Supplemental Fig. S3 H-J**). Thus, TNC induced CCL21 in LEC via integrin $\alpha 9\beta 1$.

Tenascin-C bound CCL21 and immobilized dendritic cells

Since TNC binds several soluble factors (40), it was crucial to determine whether TNC binds to CCL21. CCL21 bound to several sites within the TNC molecule whereas uncoated gold particles, or other gold-labeled molecules, not binding TNC (BSA and EGF (40)), did not interact (**Fig. 4A, B, S4A-C**). A major binding site for CCL21 was within the fibronectin type III repeats (FNIII), presumably in the 5th repeat, as CCL21 bound at the same site (5th FNIII repeat) where TGF$\beta 1$ was documented to bind TNC (40) (**Fig. 4B, Supplemental Fig. S4D**). Heparin blocked binding of CCL21 to the FNIII repeats (**Supplemental Fig. S4E**). Also, binding of CCL21 to TNC was higher at pH6 than at pH7 (**Fig. 4C**). The TNC/CCL21 binding

Author Manuscript Published OnlineFirst on July 14, 2020; DOI: 10.1158/2326-6066.CIR-20-0074
Author manuscripts have been peer reviewed and accepted for publication but have not yet been edited.

strength (Kd of 5.8 x 10^{-8} M) was lower than CCL21 binding to CCR7 but in the same range (8.4 x 10^{-8} M) (51) **(Fig. 4C**).

Using migration assays, we determined if TNC-bound CCL21 could restrain DC migration **(Supplemental Fig. S4F).** CCL21 attracted DCs in a concentration dependent manner, with fewer cells migrating toward TNC compared to FN or Col I (**Supplemental Fig. S4G**). To determine whether DC2.4 were potentially immobilized on the TNC substratum we measured cell retention by counting the cells tethered on the surface of the lower side of the insert (**Fig. 4D**). More DCs were immobilized on TNC (compared to FN or Col I) which occurred in a CCL21 dose-dependent manner and was reduced with a CCR7-blocking antibody (**Fig. 4E**). Conditioned medium (CM) from TNC-treated LEC caused DC2.4 retention on TNC compared to CM from control LECs and, this was abolished by blocking CCR7 (**Fig. 4F, S4H**).

Tenascin-C shaped an immune suppressive TME linked to increased CCR7 expression

FRC are a cellular component of reticular fibers of lymphoid tissues producing ECM and soluble factors (41). Also, cells with FRC properties (gp38+, ERTR7+, LYVE-) populate tumors (48). We wanted to know whether TNC impacted the abundance and spatial distribution of FRC. Using gp38 as marker for FRC (with CD31 negative selection) and ERTR7 staining there were more FRC in WT than TNCKO tumors (**Fig. 5A, B, S5A, B, Supplemental Table S6**).

The cellular crosstalk in lymphatic tissue is regulated by CCR7 signaling (52). There was higher *Ccr7* expression and more CCR7+ cells, in particular CCR7+ macrophages (CD11b+/F4/80+), DC (CD11c+/MHCII+), and CD8+ T cells in WT compared to TNCKO tumors (**Fig. 5C-F, Supplemental Fig. S5C-E**). CCR7+CD11c+ cells were less prominent in the local lymph nodes of WT tumor mice, again suggesting a potential role of TNC in impairing migration of these cells from the tumor site to the draining lymph nodes yet not within the lymph nodes (**Fig. 5G, Supplemental Fig. S5F).**

Author Manuscript Published OnlineFirst on July 14, 2020; DOI: 10.1158/2326-6066.CIR-20-0074
Author manuscripts have been peer reviewed and accepted for publication but have not yet been edited.

Next, we investigated whether TNC influenced the expression of CCR7. We saw higher CCR7 expression in DC2.4 upon treatment with LPS (positive control) and TNC (**Fig. 5H, S5G**). As TNC can signal through TLR4 (13) we used Cli95 to inhibit TLR4 (53) and, observed that Cli95 abolished induction of CCR7 in DC2.4 (**Fig. 5H**). Next, we asked whether TNC-induced TLR4 signaling also affected expression of the DC maturation markers CD80 and CD86. Whereas LPS increased expression of both molecules (that was blocked by Cli95), TNC did not affect their expression at the cell surface (**Supplemental Fig. S5H and I**). As we saw higher *Cd80* and *Cd86* in WT tumors we considered an effect by the tumor cells (**Supplemental Fig. S5K**). Therefore, we treated DC2.4 with CM from OSCC13 shC cells, expressing TNC (and shTNC cells with undetectable TNC) and observed higher expression of *Cd80*, *Cd86* (and *Ccr7)* supporting a paracrine mechanism of TNC action (**Fig. 5I, Supplemental Fig. S5J**). CD80 and CD86 can be induced by IL6 and TNFα (54,55) and we observed higher expression of both molecules in WT tumors (**Supplemental Fig. S5L**).

TNC also robustly increased expression of a group of genes involved in antigen processing and presentation as e.g. fifteen *MhcII* genes (H2), β2 microglobulin (*B2M*), transporter associated with antigen processing 1 (*Tap1*) and cathepsin S (*Ctss*), that were higher in WT than TNCKO tumors (**Supplemental Fig. S5K**).

Tregs (CD4+/CD25+/Foxp3+) and CCR7+ Tregs were more frequent in WT than TNCKO tumors (**Fig. 2J, 5J**). As Tregs express anti-inflammatory cytokines, we observed higher expression of the IL10 pathway (e.g. IL-10, IL1-ra, IL-1a/b) in WT tumors (**Supplemental Fig. S5M**). We observed a positive correlation between *Ccl21* expression and *Foxp3* and *Il10* expression, respectively, thus, TNC may impact Treg abundance and function through CCL21 (**Supplemental Fig. S5N**). In addition to *Tgfb1*, TNC upregulated molecules involved in Treg chemotaxis (e.g. *Ccl3, Ccl2, Rantes, Cxcl9, Cxcl10, P-selectin* and *Ccl22)* (**Fig. 5K, Supplemental Fig. S5L, O)**. High expression of these genes together with a low number of CCR7+ Treg (6%) could explain that TNC increased Treg abundance in particular within the tumor cell nests (**Fig. 2K, L)**.

Author Manuscript Published OnlineFirst on July 14, 2020; DOI: 10.1158/2326-6066.CIR-20-0074
Author manuscripts have been peer reviewed and accepted for publication but have not yet been edited.

We wondered if TNC impacted CTL abundance and activity, as DCs and Tregs can regulate CTL responses (56). Immune suppressive CD8+ Tregs and non-primed CCR7+/CD8+ T cells were more abundant in WT tumors (**Fig. 5L, Supplemental Fig. S5E**). This result suggested a potential impact of TNC on the education of CD8+ T cells in the lymph nodes and their impaired activity in tumors. In support of this idea, we saw significantly less *Ifnγ, Granzyme b* and *Perforin* expression in lymph nodes and in tumors from WT mice (**Fig. 5M, Supplemental Fig. S5P, Q**). Also, a majority of "positive T cell activation"-related genes (24 over 32) were downregulated in WT tumors **(Supplemental Fig. S5R)**. Immune-checkpoint inhibitor genes (*Pdcd1* (encoding PD1)*, Cd274* (encoding PDL-1) and *Ctla4*) and prostaglandin E2 related genes (*Ptges2, Ptgs2* and *Ptger1*) were elevated in WT compared to TNCKO tumors **(Supplemental Fig. S5L)**. Together, these data suggested an immune suppressive TME in WT tumors.

CCR7 signaling blocklade blunted the immune suppressive TME

To investigate whether enhanced CCR7 signaling by TNC was linked to immune suppression and tumor growth, we used a CCR7 blocking antibody. Carcinogen-exposed WT mice were treated with this (and a control) antibody. As shown in **Fig. 6A**, we observed less tumors. Investigating the numbers of leukocytes and immune subtypes we did not see any difference between the treated groups (**Supplemental Fig. S6A, B**). Whereas the number of CCR7+ leukocytes was not different in local lymph nodes and spleen, the number of CCR7+ DCs (CD11c+/MHCII+), macrophages (CD11b+/F4/80), Tregs (CD25+/Foxp3+) and CD8+ Tregs (CD3+/CD8+/Foxp3+) was reduced upon anti-CCR7 treatment (**Fig. 6B-E, Supplemental Fig. S6C-G**). These results precluded a systemic effect of the anti-CCR7 treatment such as a general depletion of CCR7+ cells (or other leukocytes). After anti-CCR7 treatment there were more CD45+ and CD11c+ cells in the tumor cell nests (**Fig. 6F-I**), similar to the TNCKO phenotype (**Fig. 2G-L**).

Whereas anti-CCR7 treatment did not alter CCL21 expression the expression of many anti-inflammatory molecules were reduced which was consistent with a lower abundance of Tregs (**Fig. 6D, J, Supplemental Fig. S6F, H, I**), again similar to the TNCKO phenotype (**Fig. 2J, 6K**). Addressing a potential impact of CCR7 blockade on the abundance of FRC we observed less FRC (**Fig. 6K, L**), once more mimicking the TNCKO phenotype (**Fig. 5A, B**). This was reinforced by a reduced expression of several immune suppression-related genes upon anti-CCR7 treatment, including *Mrc1* (encoding CD206) and the immune-checkpoint inhibitors *Pdcd1, Cd274* and *Ctla4* **(Supplemental Fig. S6J)**. The CCR7 antibody treatment also affected ECM-related gene expression in the tumors, notably downregulation of *Tnc* itself (**Supplemental Fig. S6K**).

Next we asked whether APC function and priming of CTL potentially was also enhanced. Indeed we saw higher IFNγ, *Granzyme b* and *Perforin* expression in the local lymph nodes and, less non-primed CD8+ T cells (CCR7+/CD3+/CD8+) inside the tumors. Higher expression of genes positively related to T cell activation upon anti-CCR7 treatment was seen (**Fig. 6E, S6L-O**). Consistently, we saw less cancer cells in the local lymph nodes of anti-CCR7 treated mice (**Supplemental Fig. S6P**).

An immune suppressive TME in human OSCC correlated with poor prognosis

To address whether immune suppression through TNC/CCL21/CCR7 is potentially relevant in human OSCC, we investigated human tumors for TNC and the LEC marker podoplanin. As the murine model mimics the early phases of the human disease, we focused on non-invasive OSCC tissue areas. Similar to the murine tumors, LEC were embedded in TNC-rich stroma (**Fig. 7A**). We co-stained the tumor tissue for CCL21 and TNC and observed CCL21 expressed in TNC-rich stroma by cells with flat nuclei forming tubes, likely representing LEC (**Fig. 7B**).

By investigating publicly available gene expression data (GSE27020), we determined expression of TNC and immune suppressive markers. High *TNC* expression (above the median) (as well as *TGFβi)* correlated with shorter time of survival until relapse (RFS), yet not with overall survival (OS) or metastasis-free survival (MFS) (**Supplemental Fig. S7A, B**). Whereas high expression of *CCR7*, *CCL21*, *Foxp3, IL-10, CD206, CTLA4* and *PD-1* alone did not correlate with shorter RFS, OS or MFS, combined high expression of all makers plus *TNC* (HR = 2.78) or *TNC* combined with *CCR7, CCL21* and *IL-10* (HR = 2.02) correlated with shorter RFS, thus supporting a potential role of TNC enforcing an immune suppressive TME in human HNSCC that favors tumor relapse (**Fig. 7C, Supplemental Fig. S7C-K**). This possibility is supported by the study of RNA Affymetrix chip data from 68 HNSCC patients (23), which shows a positive correlation between the expression of *TNC* and genes that define the immune suppressive TME (**Fig. 7D**).

Altogether, our results showed that TNC promoted a pro-tumorigenic TME with lymphoid properties by impacting FRC, CD11c+ cells, Tregs and CTLs involving integrin $\alpha 9\beta 1$ and TRL4 as well as several chemokines and cytokines which phenocopies human HNSCC (**Fig. 7E, F**).

Discussion

Fewer and smaller tongue tumors arose in absence of TNC in the 4NQO-treated mice and no invasive lesions nor lymph node invasion appeared, indicating that TNC promoted tumor progression, similar to other models (57).

TNC is expressed in TMT, also in OSCC (16, this study). Despite similarities to reticular fibers suggesting a potential role in tumor immunity, the roles of TMT were obscure (14,15). Here, TNC impacted the expression of collagens and several matrisomal molecules indicating that TNC may act as a master orchestrator of TMT.

TNC targets several immune subtypes such as CTL in models of glioblastoma and prostate cancer, macrophages in breast cancer, and CD11c+ cells and Tregs in OSCC as demonstrated here (57–59). Profound differences were observed between WT and TNCKO mice with respect to the immune cell infiltrate and expression of immune suppressive molecules in tumors and local lymph nodes. The presence of TNC led to less numerous CD11c+/MHCII+ cells in the tumor nests and enhanced their retention in the stroma. Thus, in a WT tumor, CD11c+ cells may be hampered in priming CTL due to poor migration of antigen-bearing DC to draining lymph nodes, as seen elsewhere (47,60). We observed less migratory DC in draining lymph nodes of WT tumor mice, less non-primed CCR7+ CD8+ T cells, and more poorly activated CTL in the tumors and lymph nodes of WT compared to TNCKO mice. TNC enforced infiltration of Tregs into the tumor cell nests presumably through elevated expression of Treg-attracting and maturation-promoting factors.

A role of CCL21 signaling in generating a lymphoid immuno-tolerogenic TME has previously been noticed, how this occurs remained unknown, with no link to matrix nor TNC provided (48). In our model, the natural source of CCL21 was LEC and FRC, and not the tumor cells (48). We identified CCL21/CCR7 signaling as a major target of TNC. Through induction of CCL21 in LEC (via $\alpha 9\beta 1$ integrin) and by increasing the number of FRC, a natural source of CCL21, TNC enforced a pro-tumoral TME and inverted the CCL21 gradient between lymph nodes and the tumor. This may have contributed to poor homing of CD11c+ cells and poor

activation of CTL in the lymph nodes. Inhibition of CCR7 abolished the immune suppressive properties of the TME and subsequently reduced tumor number, tumor progression and lymph node metastasis.

Our observations supported a dual function of TNC in tumor immunity, in which its ancient role as DAMP and as a component of reticular fibers may be exploited by tumors (10,13,17). CCR7 blockade phenocopied features of the TNCKO supporting a causal link between TNC and CCR7.

In human OSCC, CCL21 induction by TNC in LEC may be relevant as high expression of TNC in conjunction with CCR7, CCL21 and other immune suppressive markers correlated with shorter RFS. Our results could improve HNSCC diagnosis and therapy such as using Raman microspectroscopy for detection of stromal CCL21. Approximately 80% of patients with combined low expression of *TNC* and the immune suppressive markers survived longer than 5 years and may represent a group that would benefit from a less harsh treatment.

DCs were released from the TNC/CCL21 substratum upon CCR7 inhibition suggesting a potential role of CCR7 as co-receptor of β2 integrins expressed on DCs (61). Thus, targeting β2 integrins (62) could be relevant in releasing CD11c+ cells from the matrix. Also targeting CCR7 may be useful because of its profound effect on abolishing the immune suppressive properties of the TME, but not altering general immunity. CCR7 is a target in lymphomas and several metastatic cancers, but not yet in HNSCC (63). Several CCR7 targeting approaches have been developed (64-67) that could be tested in HNSCC. We have shown that targeting CCR7 appears to be safe and efficient.

TNC regulated the crosstalk of immune cells with CCL21, the positioning of TIL, especially CD11c+ cells and Tregs and, subsequently reduced adaptive immunity, thereby facilitating escape from immunosurveillance. Blockade of CCL21/CCR7 signaling relieved the pro-tumoral immune suppressive properties of the TME, normalized features of the tumor bed and reduced tumorigenesis and metastasis thus, providing novel targeting opportunities.

Acknowledgements

We thank O. Lefebvre, F. Steinbach, A. Klein, C. Arnold, and the animal facility for technical support, A. Molitor and A. Pichot for RNA sequencing, K. Schlattmann, C. Alampi, M. Chami, and K. Qvortrup for EM imaging assistence, N. Toussan for CD45 immunostaining, and A. Jung for access to gene expression data. Supported by grants from INCa, Ligue National Contre le Cancer and the Foundation ARC (PAIR-VADS11-023: EVO and GO) and AAP2017.LNCC/EVO (EVO, FA, and GO) and the Ligue Régionale contre le Cancer, INSERM and University Strasbourg (to GO), and Cancéropôle PACA and LABEX SIGNALIFE program (ANR-11-LABEX-0028-01: EVO and FA); Deutsche Forschungsgemeinschaft (EXC 2180, INST 2388/64-1), Ministry of Science, Research and Arts of Baden Württemberg (Az.: SI-BW 01222-91, 33-729.55-3/214-8 (to KS-L and EMB), and fellowship grants from French Ministry of Research MRT (to WE) and Fondation ARC (to DM).

Authors contribution

CS established and characterized the carcinogen model, CS and TL applied and investigated the model. CS, TL, DM, WE, SBFD, LP, PB, RV, MM, GC, EMB, VR, AC, UH, SS, KN, SR, TI, NP, RC, NP, KH, HD, CM, MK and KSL performed experiments, analyzed and interpreted the data. The following experiments were performed by the mentioned authors: SRP by GC, negative EM imaging by MM, EM imaging by UH, Raman microspectroscopy by EMB and KSL, RNA seq analysis by NP and RC, proteomics experiments by AH, NP and CC, migration assays, Kaplan Meier analysis and treatment of mice with anti-CCR7 by TL, FACS analysis by TL, RV, LP and HD, FRC isolation by TL, AC and CM, tissue staining by TL, CS, DM and WE, preparation of murine TNC by TI and MK, preparation of human TNC by DD and WE, generation of the integrin $\alpha 9\beta 1$ specific antibody by SK. AS and EVO supervised the analysis of the human HNSCC tissues. CS, TL, EVO and GO wrote the manuscript. EVO, FA, CS, TL and GO conceptualized and GO supervised the study. Grants to FA, EVO and GO largely financed the work.

Disclosure of potential conflict of interest

The authors declare no competing financial interests.

References

1. Sacco AG, Cohen EE. Current Treatment Options for Recurrent or Metastatic Head and Neck Squamous Cell Carcinoma. J Clin Oncol. 2015 Oct 10;33(29):3305–13.
2. Leemans CR, Braakhuis BJM, Brakenhoff RH. The molecular biology of head and neck cancer. Nat Rev Cancer. 2011 Jan;11(1):9–22.
3. Ferris RL. Immunology and Immunotherapy of Head and Neck Cancer. J Clin Oncol. 2015 Oct 10;33(29):3293–304.
4. Seiwert TY, Burtness B, Mehra R, Weiss J, Berger R, Eder JP, et al. Safety and clinical activity of pembrolizumab for treatment of recurrent or metastatic squamous cell carcinoma of the head and neck (KEYNOTE-012): an open-label, multicentre, phase 1b trial. Lancet Oncol. 2016 Jul;17(7):956–65.
5. Langlois B, Saupe F, Rupp T, Arnold C, van der Heyden M, Orend G, et al. AngioMatrix, a signature of the tumor angiogenic switch-specific matrisome, correlates with poor prognosis for glioma and colorectal cancer patients. Oncotarget. 2014 Oct 7;5(21):10529–45.
6. Maziveyi M, Alahari SK. Cell matrix adhesions in cancer: The proteins that form the glue. Oncotarget. 2017 Apr 20;8(29):48471–87.
7. Turley SJ, Cremasco V, Astarita JL. Immunological hallmarks of stromal cells in the tumour microenvironment. Nat Rev Immunol. 2015 Nov;15(11):669–82.
8. Van Obberghen-Schilling E, Tucker RP, Saupe F, Gasser I, Cseh B, Orend G. Fibronectin and tenascin-C: accomplices in vascular morphogenesis during development and tumor growth. Int J Dev Biol. 2011;55(4–5):511–25.
9. Chiquet-Ehrismann R, Orend G, Chiquet M, Tucker RP, Midwood KS. Tenascins in stem cell niches. Matrix Biology. 2014 Jul 1;37:112–23.
10. Midwood KS, Hussenet T, Langlois B, Orend G. Advances in tenascin-C biology. Cell Mol Life Sci. 2011 Oct;68(19):3175–99.
11. Midwood KS, Chiquet M, Tucker RP, Orend G. Tenascin-C at a glance. J Cell Sci. 2016 Dec 1;129(23):4321–7.
12. Imanaka-Yoshida K, Aoki H. Tenascin-C and mechanotransduction in the development and diseases of cardiovascular system. Front Physiol [Internet]. 2014 Jul 29 [cited 2019 Aug 10];5. Available from: https://www.ncbi.nlm.nih.gov/pmc/articles/PMC4114189/
13. Midwood K, Sacre S, Piccinini AM, Inglis J, Trebaul A, Chan E, et al. Tenascin-C is an endogenous activator of Toll-like receptor 4 that is essential for maintaining inflammation in arthritic joint disease. Nat Med. 2009 Jul;15(7):774–80.
14. Drumea-Mirancea M, Wessels JT, Müller CA, Essl M, Eble JA, Tolosa E, et al. Characterization of a conduit system containing laminin-5 in the human thymus: a potential transport system for small molecules. J Cell Sci. 2006 Apr 1;119(7):1396–405.
15. Spenlé C, Saupe F, Midwood K, Burckel H, Noel G, Orend G. Tenascin-C: Exploitation and collateral damage in cancer management. Cell Adh Migr. 2015;9(1–2):141–53.
16. Rupp T, Langlois B, Koczorowska MM, Radwanska A, Sun Z, Hussenet T, et al. Tenascin-C Orchestrates Glioblastoma Angiogenesis by Modulation of Pro- and Anti-angiogenic Signaling. Cell Reports. 2016 Dec;17(10):2607–19.

17. Spenlé C, Gasser I, Saupe F, Janssen K-P, Arnold C, Klein A, et al. Spatial organization of the tenascin-C microenvironment in experimental and human cancer. Cell Adh Migr. 2015 Jan 22;9(1–2):4–13.
18. Sun Z, Velázquez-Quesada I, Murdamoothoo D, Ahowesso C, Yilmaz A, Spenlé C, et al. Tenascin-C increases lung metastasis by impacting blood vessel invasions. Matrix Biol. 2019 Jul 6;
19. Gopal S, Veracini L, Grall D, Butori C, Schaub S, Audebert S, et al. Fibronectin-guided migration of carcinoma collectives. Nat Commun. 2017 Jan 19;8:14105.
20. Foy J-P, Tortereau A, Caulin C, Le Texier V, Lavergne E, Thomas E, et al. The dynamics of gene expression changes in a mouse model of oral tumorigenesis may help refine prevention and treatment strategies in patients with oral cancer. Oncotarget. 2016 Mar 24;7(24):35932–45.
21. Wang Z, Wu VH, Allevato MM, Gilardi M, He Y, Luis Callejas-Valera J, et al. Syngeneic animal models of tobacco-associated oral cancer reveal the activity of in situ anti-CTLA-4. Nat Commun. 2019 05;10(1):5546.
22. Goswami CP, Nakshatri H. PROGgeneV2: enhancements on the existing database. BMC Cancer [Internet]. 2014 Dec 17 [cited 2019 Aug 5];14. Available from: https://www.ncbi.nlm.nih.gov/pmc/articles/PMC4300843/
23. Jung AC, Job S, Ledrappier S, Macabre C, Abecassis J, Reyniès A de, et al. A Poor Prognosis Subtype of HNSCC Is Consistently Observed across Methylome, Transcriptome, and miRNome Analysis. Clin Cancer Res. 2013 Aug 1;19(15):4174–84.
24. Benjamini Y, Drai D, Elmer G, Kafkafi N, Golani I. Controlling the false discovery rate in behavior genetics research. Behav Brain Res. 2001 Nov 1;125(1–2):279–84.
25. Talts JF, Wirl G, Dictor M, Muller WJ, Fässler R. Tenascin-C modulates tumor stroma and monocyte/macrophage recruitment but not tumor growth or metastasis in a mouse strain with spontaneous mammary cancer. J Cell Sci. 1999 Jun;112 (Pt 12):1855–64.
26. Somovilla-Crespo B, Alfonso-Pérez M, Cuesta-Mateos C, Carballo-de Dios C, Beltrán AE, Terrón F, et al. Anti-CCR7 therapy exerts a potent anti-tumor activity in a xenograft model of human mantle cell lymphoma. J Hematol Oncol. 2013 Dec 4;6:89.
27. Dobin A, Davis CA, Schlesinger F, Drenkow J, Zaleski C, Jha S, et al. STAR: ultrafast universal RNA-seq aligner. Bioinformatics. 2013 Jan 1;29(1):15–21.
28. Langmead B, Salzberg SL. Fast gapped-read alignment with Bowtie 2. Nat Methods. 2012 Mar 4;9(4):357–9.
29. Anders S, Pyl PT, Huber W. HTSeq--a Python framework to work with high-throughput sequencing data. Bioinformatics. 2015 Jan 15;31(2):166–9.
30. Love MI, Huber W, Anders S. Moderated estimation of fold change and dispersion for RNA-seq data with DESeq2. Genome Biol. 2014;15(12):550.
31. Mi H, Huang X, Muruganujan A, Tang H, Mills C, Kang D, et al. PANTHER version 11: expanded annotation data from Gene Ontology and Reactome pathways, and data analysis tool enhancements. Nucleic Acids Res. 2017 04;45(D1):D183–9.
32. Fabregat A, Sidiropoulos K, Viteri G, Forner O, Marin-Garcia P, Arnau V, et al. Reactome pathway analysis: a high-performance in-memory approach. BMC Bioinformatics. 2017 Mar 2;18(1):142.
33. Tyanova S, Temu T, Cox J. The MaxQuant computational platform for mass spectrometry-based shotgun proteomics. Nat Protoc. 2016 Dec;11(12):2301–19.
34. Wieczorek S, Combes F, Lazar C, Giai Gianetto Q, Gatto L, Dorffer A, et al. DAPAR & ProStaR: software to perform statistical analyses in quantitative discovery proteomics. Bioinformatics. 2017 Jan 1;33(1):135–6.

35. Ritchie ME, Phipson B, Wu D, Hu Y, Law CW, Shi W, et al. limma powers differential expression analyses for RNA-sequencing and microarray studies. Nucleic Acids Res. 2015 Apr 20;43(7):e47.
36. Huang W, Chiquet-Ehrismann R, Moyano JV, Garcia-Pardo A, Orend G. Interference of tenascin-C with syndecan-4 binding to fibronectin blocks cell adhesion and stimulates tumor cell proliferation. Cancer Res. 2001 Dec 1;61(23):8586–94.
37. Giblin SP, Murdamoothoo D, Deligne C, Schwenzer A, Orend G, Midwood KS. How to detect and purify tenascin-C. Methods Cell Biol. 2018;143:371–400.
38. Bober M, Enochsson C, Collin M, Mörgelin M. Collagen VI is a subepithelial adhesive target for human respiratory tract pathogens. J Innate Immun. 2010;2(2):160–6.
39. Baschong W, Wrigley NG. Small colloidal gold conjugated to Fab fragments or to immunoglobulin G as high-resolution labels for electron microscopy: a technical overview. J Electron Microsc Tech. 1990 Apr;14(4):313–23.
40. De Laporte L, Rice JJ, Tortelli F, Hubbell JA. Tenascin C Promiscuously Binds Growth Factors via Its Fifth Fibronectin Type III-Like Domain. Engler AJ, editor. PLoS ONE. 2013 Apr 18;8(4):e62076.
41. Fletcher AL, Acton SE, Knoblich K. Lymph node fibroblastic reticular cells in health and disease. Nat Rev Immunol. 2015 Jun;15(6):350–61.
42. Elmusrati AA, Pilborough AE, Khurram SA, Lambert DW. Cancer-associated fibroblasts promote bone invasion in oral squamous cell carcinoma. British Journal of Cancer. 2017 Sep;117(6):867–75.
43. Shivamallappa SM, Venkatraman NT, Shreedhar B, Mohanty L, Shenoy S. Role of angiogenesis in oral squamous cell carcinoma development and metastasis: an immunohistochemical study. Int J Oral Sci. 2011 Oct;3(4):216–24.
44. Saupe F, Schwenzer A, Jia Y, Gasser I, Spenlé C, Langlois B, et al. Tenascin-C Downregulates Wnt Inhibitor Dickkopf-1, Promoting Tumorigenesis in a Neuroendocrine Tumor Model. Cell Reports. 2013 Oct;5(2):482–92.
45. Naba A, Clauser KR, Hoersch S, Liu H, Carr SA, Hynes RO. The matrisome: in silico definition and in vivo characterization by proteomics of normal and tumor extracellular matrices. Mol Cell Proteomics. 2012 Apr;11(4):M111.014647.
46. Baaten B, Tinoco R, Chen A, Bradley L. Regulation of Antigen-Experienced T Cells: Lessons from the Quintessential Memory Marker CD44. Front Immunol [Internet]. 2012 [cited 2020 Apr 10];3. Available from: https://www.frontiersin.org/articles/10.3389/fimmu.2012.00023/full
47. Hervouet C, Luci C, Rol N, Rousseau D, Kissenpfennig A, Malissen B, et al. Langerhans cells prime IL-17-producing T cells and dampen genital cytotoxic responses following mucosal immunization. J Immunol. 2010 May 1;184(9):4842–51.
48. Shields JD, Kourtis IC, Tomei AA, Roberts JM, Swartz MA. Induction of lymphoidlike stroma and immune escape by tumors that express the chemokine CCL21. Science. 2010 May 7;328(5979):749–52.
49. Kozai M, Kubo Y, Katakai T, Kondo H, Kiyonari H, Schaeuble K, et al. Essential role of CCL21 in establishment of central self-tolerance in T cells. J Exp Med. 2017 Jul 3;214(7):1925–35.
50. Frohwitter G, Buerger H, Van diest PJ, Korsching E, Kleinheinz J, Fillies T. Cytokeratin and protein expression patterns in squamous cell carcinoma of the oral cavity provide evidence for two distinct pathogenetic pathways. Oncol Lett. 2016 Jul;12(1):107–13.
51. Lanati S, Dunn DB, Roussigné M, Emmett MS, Carriere V, Jullien D, et al. Chemotrap-1: an engineered soluble receptor that blocks chemokine-induced migration of metastatic cancer cells in vivo. Cancer Res. 2010 Oct 15;70(20):8138–48.

52. Förster R, Schubel A, Breitfeld D, Kremmer E, Renner-Müller I, Wolf E, et al. CCR7 coordinates the primary immune response by establishing functional microenvironments in secondary lymphoid organs. Cell. 1999 Oct 1;99(1):23–33.
53. Wang H, Mo L, Xiao X, An S, Liu X, Ba J, et al. Pplase of Dermatophagoides farinae promotes ovalbumin-induced airway allergy by modulating the functions of dendritic cells in a mouse model. Scientific Reports. 2017 Feb 27;7(1):43322.
54. Trevejo JM, Marino MW, Philpott N, Josien R, Richards EC, Elkon KB, et al. TNF-α-dependent maturation of local dendritic cells is critical for activating the adaptive immune response to virus infection. PNAS. 2001 Oct 9;98(21):12162–7.
55. Park S-J, Nakagawa T, Kitamura H, Atsumi T, Kamon H, Sawa S, et al. IL-6 Regulates In Vivo Dendritic Cell Differentiation through STAT3 Activation. The Journal of Immunology. 2004 Sep 15;173(6):3844–54.
56. Osorio F, Fuentes C, López MN, Salazar-Onfray F, González FE. Role of Dendritic Cells in the Induction of Lymphocyte Tolerance. Front Immunol [Internet]. 2015 Oct 20 [cited 2020 Jun 22];6. Available from: https://www.ncbi.nlm.nih.gov/pmc/articles/PMC4611163/
57. Deligne C, Murdamoothoo D, Gammage AN, Gschwandtner M, Erne W, Loustau T, et al. Matrix-targeting immunotherapy controls tumor growth and spread by switching macrophage phenotype. Cancer Immunol Res. 2020 Jan 15;
58. Huang J-Y, Cheng Y-J, Lin Y-P, Lin H-C, Su C-C, Juliano R, et al. Extracellular Matrix of Glioblastoma Inhibits Polarization and Transmigration of T Cells: The Role of Tenascin-C in Immune Suppression. The Journal of Immunology. 2010 Aug 1;185(3):1450–9.
59. Jachetti E, Caputo S, Mazzoleni S, Brambillasca CS, Parigi SM, Grioni M, et al. Tenascin-C Protects Cancer Stem-like Cells from Immune Surveillance by Arresting T-cell Activation. Cancer Res. 2015 May 15;75(10):2095–108.
60. Tamoutounour S, Henri S, Lelouard H, de Bovis B, de Haar C, van der Woude CJ, et al. CD64 distinguishes macrophages from dendritic cells in the gut and reveals the Th1-inducing role of mesenteric lymph node macrophages during colitis. Eur J Immunol. 2012 Dec;42(12):3150–66.
61. Schittenhelm L, Hilkens CM, Morrison VL. β2 Integrins As Regulators of Dendritic Cell, Monocyte, and Macrophage Function. Front Immunol [Internet]. 2017 Dec 20 [cited 2019 Jun 3];8. Available from: https://www.ncbi.nlm.nih.gov/pmc/articles/PMC5742326/
62. Raab-Westphal S, Marshall JF, Goodman SL. Integrins as Therapeutic Targets: Successes and Cancers. Cancers (Basel) [Internet]. 2017 Aug 23 [cited 2020 Apr 9];9(9). Available from: https://www.ncbi.nlm.nih.gov/pmc/articles/PMC5615325/
63. Mollica Poeta V, Massara M, Capucetti A, Bonecchi R. Chemokines and Chemokine Receptors: New Targets for Cancer Immunotherapy. Front Immunol [Internet]. 2019 Mar 6 [cited 2019 Oct 31];10. Available from: https://www.ncbi.nlm.nih.gov/pmc/articles/PMC6414456/
64. Cunningham H, Kim E, August K, Vines C. Novel single chain antibodies to inhibit ccr7 mediated-entry of pediatric t-cell acute lymphoblastic leukemia into the CNS. Ann Oncol. 2014 Sep 1;25(suppl_4):iv328–iv328.
65. Jakobs BD, Spannagel L, Purvanov V, Uetz-von Allmen E, Matti C, Legler DF. Engineering of Nanobodies Recognizing the Human Chemokine Receptor CCR7. Int J Mol Sci. 2019 May 27;20(10).
66. Liu J, Wei Y, Luo Q, Xu F, Zhao Z, Zhang H, et al. Baicalin attenuates inflammation in mice with OVA-induced asthma by inhibiting NF-κB and suppressing

CCR7/CCL19/CCL21. International Journal of Molecular Medicine. 2016 Nov 1;38(5):1541–8.
67. Chi B-J, Du C-L, Fu Y-F, Zhang Y-N, Wang RW. Silencing of CCR7 inhibits the growth, invasion and migration of prostate cancer cells induced by VEGFC. Int J Clin Exp Pathol. 2015;8(10):12533–40.

Figure legends

Figure 1) TNC expression in human and murine OSCC tissue and its impact on tumorigenesis in a 4NQO-induced OSCC model

Representative (of more than 30) images of IHC staining for TNC **(A)** and CD45 **(B)** in human OSCC (tongue tumor). **(C)** Differential spatial distribution of leukocytes in human OSCC. Quantification of CD45+ leukocytes in the tumor epithelial nests and stroma, (N = 10 tumors, 3 regions per tumor). **(D)** Representative composite images of H&E stained cross sections (N = 19) from tongues of 4NQO-treated WT and TNCKO mice. The black arrows and circles indicate the tongue tumor. **(E)** Representative images (N = 19) of IF staining as indicated the nontumoral and tumoral areas of a 4NQO-induced tongue lesion. Quantification of tongue tumor number **(F)** and size **(G)** in WT and TNCKO mice. **(F),** N = 19 mice per group, **(G),** N = 6 (WT) and N = 7 (KO) mice, n = 8-10 images per tongue. **(H)** Tongue tumor classification in WT and TNCKO mice. Lesions from WT and TNCKO mice (n = 19 per genotype), differentiated squamous cell carcinoma (black), in situ carcinoma expressing keratin (grey) or invasive carcinoma (white). T = tumor cell nest, S = stroma. **(I, J)** Detection and quantification of mandibular lymph node metastasis in WT and TNCKO tumor mice. **(I)** Representative of 20 images of lymph node tissue after hematoxylin-eosin and p63/laminin staining. **(J)** Quantification of p63 positive area (%) per image. 5 images per lymph node, N = 9 mice per genotype. Mean, +/- SEM, T-test, *** $p < 0.005$ **(C),** Mann-Whitney test, ** $p < 0.01$ **(F),** * $p < 0.05$ **(G, J).** Scale bar, 50µm **(E)**, 100µm **(A, I)**, 200 µm **(B)**, 1000 µm **(D)**.

Figure 2) TNC impacted tumor stroma organization and abundance and spatial distribution of immune cells

(A, B) Raman microspectroscopic analysis of the ECM in WT and TNCKO tongue tumors. Significant differences of ECM in WT and TNCKO tumors were identified in single wave numbers 770, 820, 880 and 960 cm-1 which are assigned to collagens indicating differences in collagen fiber network **(A)** and in PC1 score values **(B)**. N = 3 per genotype. Mean ± SEM, Mann-Whitney test, * p = 0.018. **(C, E, H, K)** Representative IF images (of at least 48) for the indicated molecules in 4NQO WT and TNCKO tumors. **(D, G, J)** Representation of the indicated cell type abundance as determined by flow cytometry. N = 6 WT and N = 7 KO mice (one tumor per mouse). **(F, I, L)** Quantification of immunostaining results to evaluate the spatial distribution of the indicated cells expressed as a ratio (percentage) of positive cells over the total of cells in the tumor nest per image. **(B, D, F, G, I, J, L)** Mean values (± SEM), 4 mice per genotype, 8-10 images per tumor. Mean ± SEM, Mann-Whitney test * $p < 0.05$, ** $p < 0.01$. T = Tumor cell nest (p63+); S = Stroma, (p63-). Scale bar 400µm **(C)**, 100 µm (**E, H, K**).

Figure 3) TNC upregulated CCL21 in lymphatic endothelial cells

(A) Representative picture (one of two) of the proteome profiler array of 4NQO WT and TNCKO tumors. Pixel density represents protein expression. N = 5 tumors pooled per condition (2 replicates). **(B)** Gene expression analysis (qRTPCR) of *Ccl21* in tongue tumors of WT and TNCKO mice (N = 5 per genotype). **(C)** Quantification of CCL21 protein by ELISA in tongue tumors and draining lymph nodes from WT and TNCKO mice. N = 6 per group. **(D)** Raman microscopy of CCL21 in the stroma of WT and TNCKO tumors. Areas of TMTs were identified and scanned (Black box). Representative of 9 Raman images of ECM (red) and CCL21 (green) for WT and TNCKO tumors. **(E)** Raman spectra from lung and mandibular lymph node (LN) of control mice, WT and TNCKO tumors**. (F)** Raman quantification of CCL21 pixel intensities in stroma of WT and TNCKO tumors. N = 3 tumors per genotype. **(G, I)** Representative of 40 IF images for the indicated molecules in a WT and TNCKO tumor. **(H)** Score determination of CCL21 in WT (N = 5) and TNCKO (N = 5) tumors, 8-10 images per tumor. **(J, K)** ELISA for CCL21 in CM from OSCC13 and FRC cells **(J)** or LEC **(K)**, either

non-stimulated (NS) or stimulated with TNC in the presence of the indicated inhibitors **(K).** N = 5 **(J)** and 3 **(K)** independent experiments. **(B, F, H, K)** Mean ± SEM. Mann-Whitney test, * $p < 0.05$; Kruskal-Wallis test and Dunn's post-test. * $p < 0.05$, ** $p < 0.01$ **(C, J)**. Scale bar, 30 µm **(D)**, 100 µm **(G, I)**.

Figure 4) TNC bound CCL21, leading to dendritic cell retention

(A, B) Binding of gold-labeled CCL21 to murine TNC determined by negative staining and transmission electron microscopy. **(A)** Representative of 500 micrographs, **(B)** quantification of bound CCL21 particles along the length of the TNC monomer. Scale bars: 100 nm (left), 50 nm (right). **(C)** Binding of soluble CCL21 to TNC as measured by surface plasmon resonance spectrometry. Kd (1/s) = 0.0231; KD (M) = 6.78e-08; KA (1/M) = 1.47e+07. **(D)** Schematic representation of the Boyden chamber transwell chemoretention assay of DC2.4 towards a gradient of CCL21 or conditioned medium (CM) of LEC upon treatment with human TNC. The lower surface of the insert was coated with FN, Col I or human TNC. **(E, F)** Quantification of DC2.4 on the coated surface upon migration towards CCL21 (µg/ml, 5 hours) **(E)** or CM (8 hours) **(F)** and pre-treatment (+) or not (-) with a CCR7 antibody. NS, unstimulated. N = 4 experiments (8 wells) with 5 images per well. Mean ± SEM, Kruskal-Wallis test and Dunn's post-test. * $p < 0.05$, *** $p < 0.005$ (relative to FN and Col I coating); ## $p < 0.01$, ### $p < 0.005$ (relative to CCR7 Ab- condition); ∂∂∂ $p < 0.001$ (relative to NS condition).

Figure 5) Immune suppressive and lymphoid properties of TNC-rich stroma in the murine OSCC

(A, C) Representative of 20 IF images for the indicated molecules in WT and TNCKO tumors. Arrow points at signal. Quantification of cells by flow cytometry with the indicated antibodies in tumors **(B, E, F, J, L)** and lymph nodes **(G)**, WT (N = 6) and TNCKO (N = 7). **(D)** Score measurement of CCR7 in tongue tumors of WT and TNCKO mice, 5 mice per genotype, 8-10 images per tumor. **(H)** CCR7 expression analysis in DC2.4 cells by flow cytometry (% of viable cells) treated *in vitro* with the indicated conditions. NS, medium alone.

5 experiments. **(I)** Expression of the indicated molecules by qRTPCR upon treatment with CM as indicated. **(K)** Expression of IL-10 signaling pathway-related molecules (most deregulated) in pooled WT and TNCKO tumors (5 per condition) determined with a proteome profiler array in duplicate (two membranes per condition), $p = 1.11 \times 10^{-16}$. **(M)** Quantification of IFNγ protein by ELISA in the tumor and regional lymph nodes of the neck form WT and TNCKO mice. N = 5 per tissue and group. Mean ± SEM, Mann-Whitney test **(B, D, E, F, G, I, J)**; Mean ± SEM, Kruskal-Wallis test and Dunn's post-test **(H, M)**. , * $p < 0.05$, ** $p < 0.01$, *** $p < 0.005$. Scale bar, 100 µm **(A, C)**.

Figure 6) CCR7 inhibition abolished the immune suppressive phenotype mimicking TNCKO tumors

(A) Quantification of tongue tumor number in Control Ab and CCR7 Ab treated WT mice**,** N = 5 mice per group. **(B-E, L)** Flow cytometry quantification of cells upon treatment of tumor bearing WT mice with anti-CCR7 antibody (N = 5) or isotype control antibody (N = 5) as indicated. **(F-I, K)** Spatial distribution of cells and ECM in anti-CCR7 treated tumors as determined by IF **(F, H, K)** and quantification **(G, I)**. **(F, H, K)** Representative images of 20 are shown or IF stainings as indicated. **(G, I)** Quantification of the indicated cells in the tumor cell nests, mean values from 4 tumors per genotype, 8-10 random images per tumor. **(J)** Heatmap representation of a proteome profiler array for IL-10 signaling pathway-related molecules in anti-CCR7 treated tumors. N = 5 tumors pooled per group, experiment done in duplicate (two membranes per group). **(M)** Quantification of IFNγ protein by ELISA in the regional lymph nodes of the neck in anti-CCR7 treated mice. Mean ± SEM, Mann-Whitney test, * $p < 0.05$, ** $p < 0.01$ **(A – E, G, I, L, M).** Scale bar, 100 µm **(F, H, K).**

Figure 7) TNC enforced an immune suppressive TME in human OSCC

(A) Representative IHC staining images for podoplanin and TNC in serial whole sections of a human tongue OSCC (N = 102). Scale bar = 1000 µm (on the top images) and 50 µm (on the bottom images). **(B)** Representative images of 40 IF staining for CCL21 and TNC in a section

of a human tongue OSCC (N = 4). Scale bar = 40 µm (image on the left) and 20µm (image on the right). **(C)** Kaplan Meier analysis of HNSCC patient (GSE27020) survival until tumor relapse and combined expression of the indicated molecules above or below the median. Hazard ratio (HR) = 2.78; p = 0.011; n = 54 per cohort. **(D)** Corrplot package analysis for visualization of the correlation matrix between TNC and the indicated genes in HNSCC patients. The values in the circles are the adjusted p-values and the color intensities correspond to spearman correlation values. Adjusted p-values below 0.01 are annotated as 0. **(E)** TNC enforced an immune suppressive protumoral TME with lymphoid properties, thereby promoting tumor growth and progression in OSCC. TNC regulated abundance and the spatial distribution of Tregs (inside the tumor cell nest) and CD11c+/DC (inside the stroma). Through binding to CCL21, TNC turned into an adhesive substratum immobilizing CD11c+/DC (through CCR7 signaling), thus impairing DC migration to the regional lymph nodes, compromising adaptive immunity. **(F)** In addition to increasing the abundance of FRC, a natural source of CCL21, TNC also induced expression of CCL21 in LEC (through integrin $\alpha 9\beta 1$). TNC also increased CCR7 in DC (through TLR4) thereby enforcing stromal immobilization of DC. CCR7 blockade reduced tumor growth and progression.

Figure 1

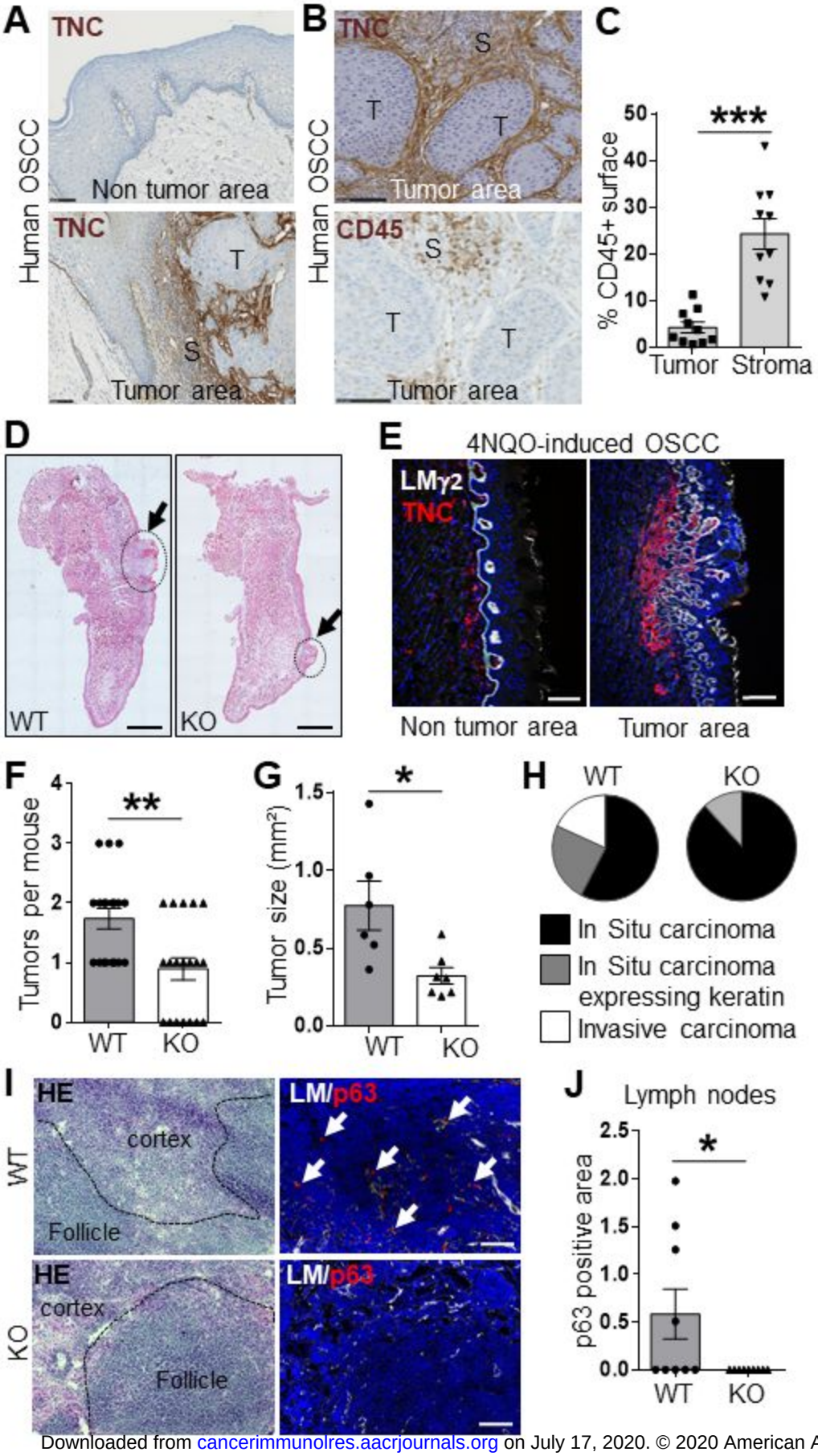

Figure 2

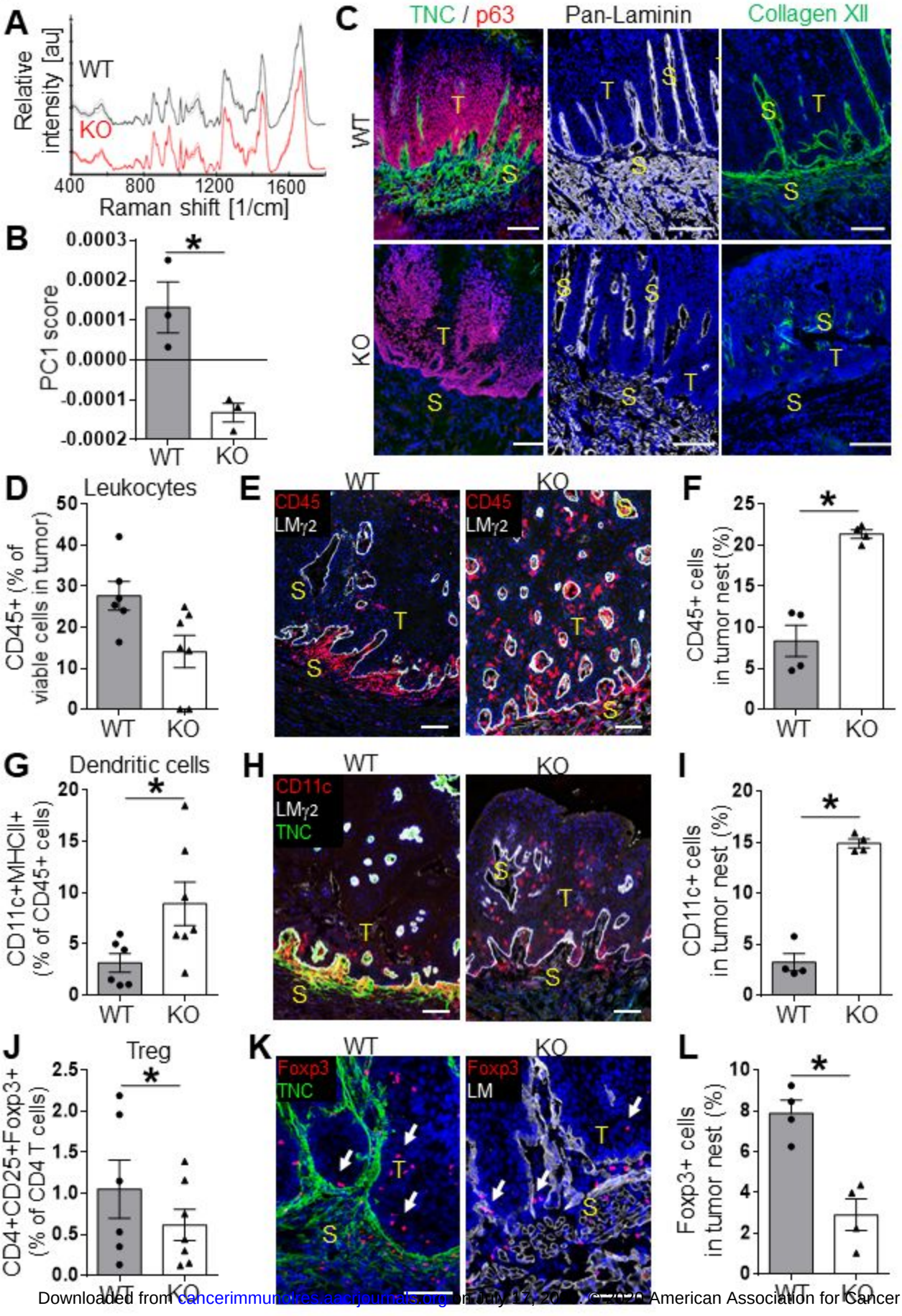

Figure 3

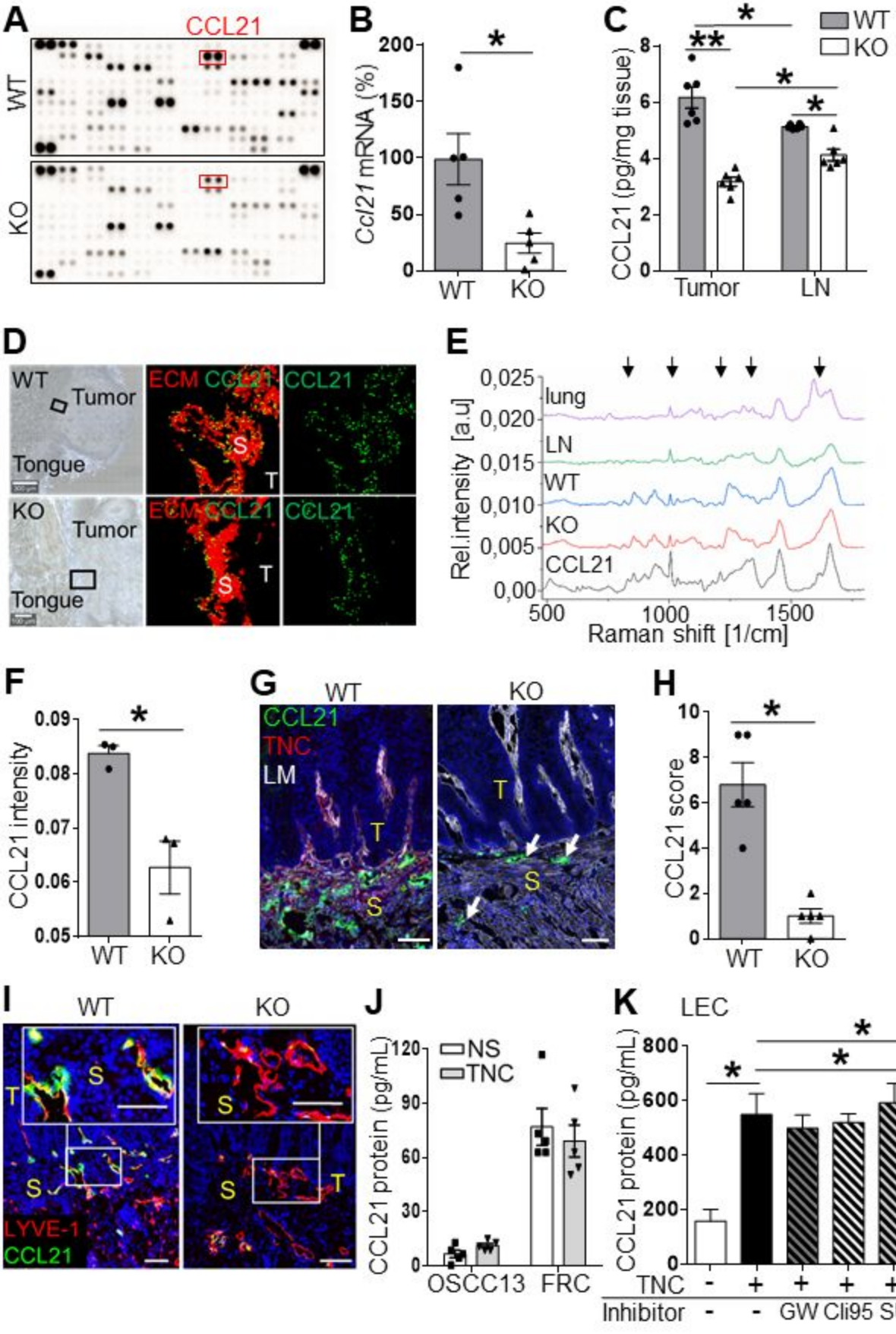

Figure 4

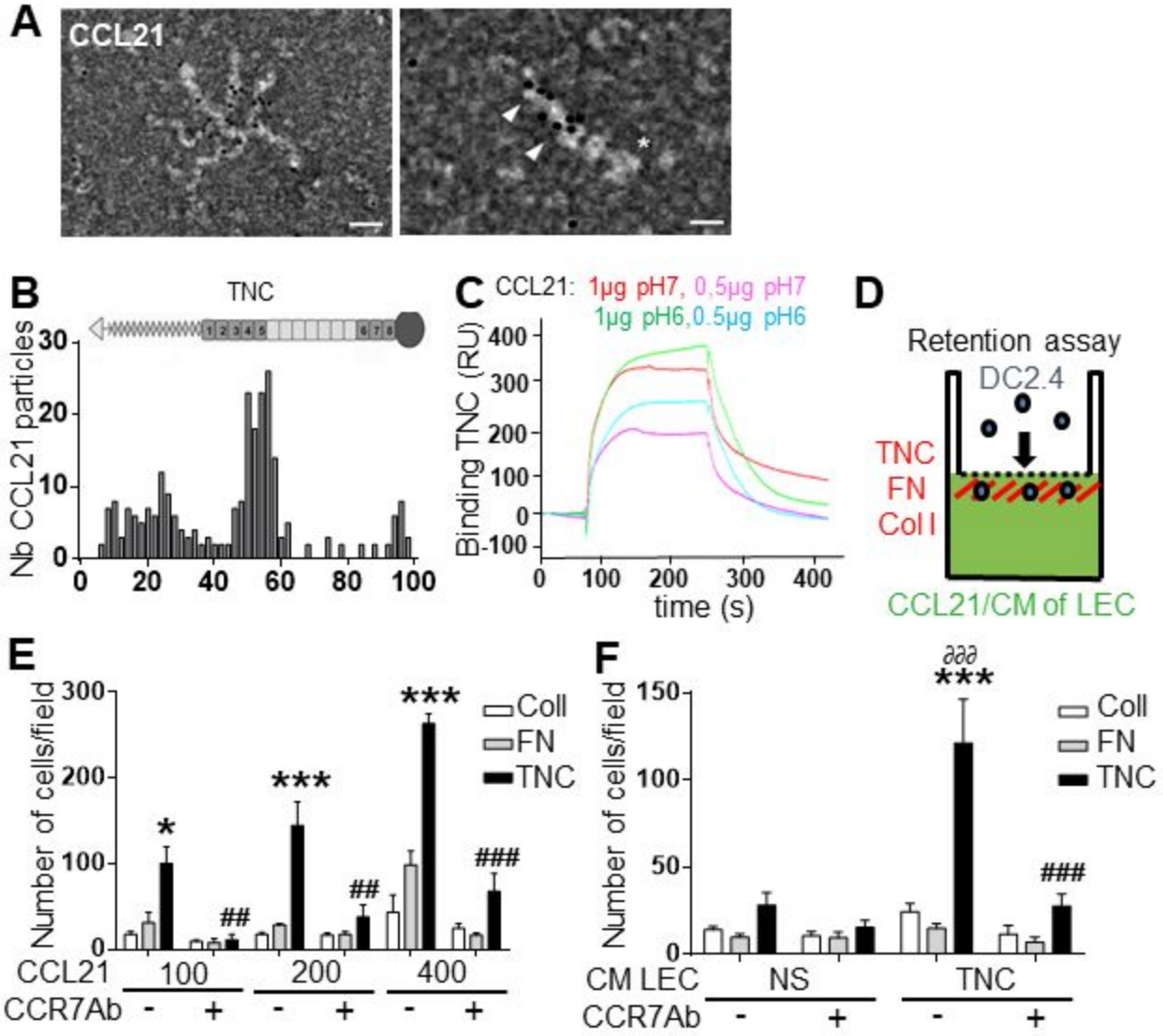

Figure 5

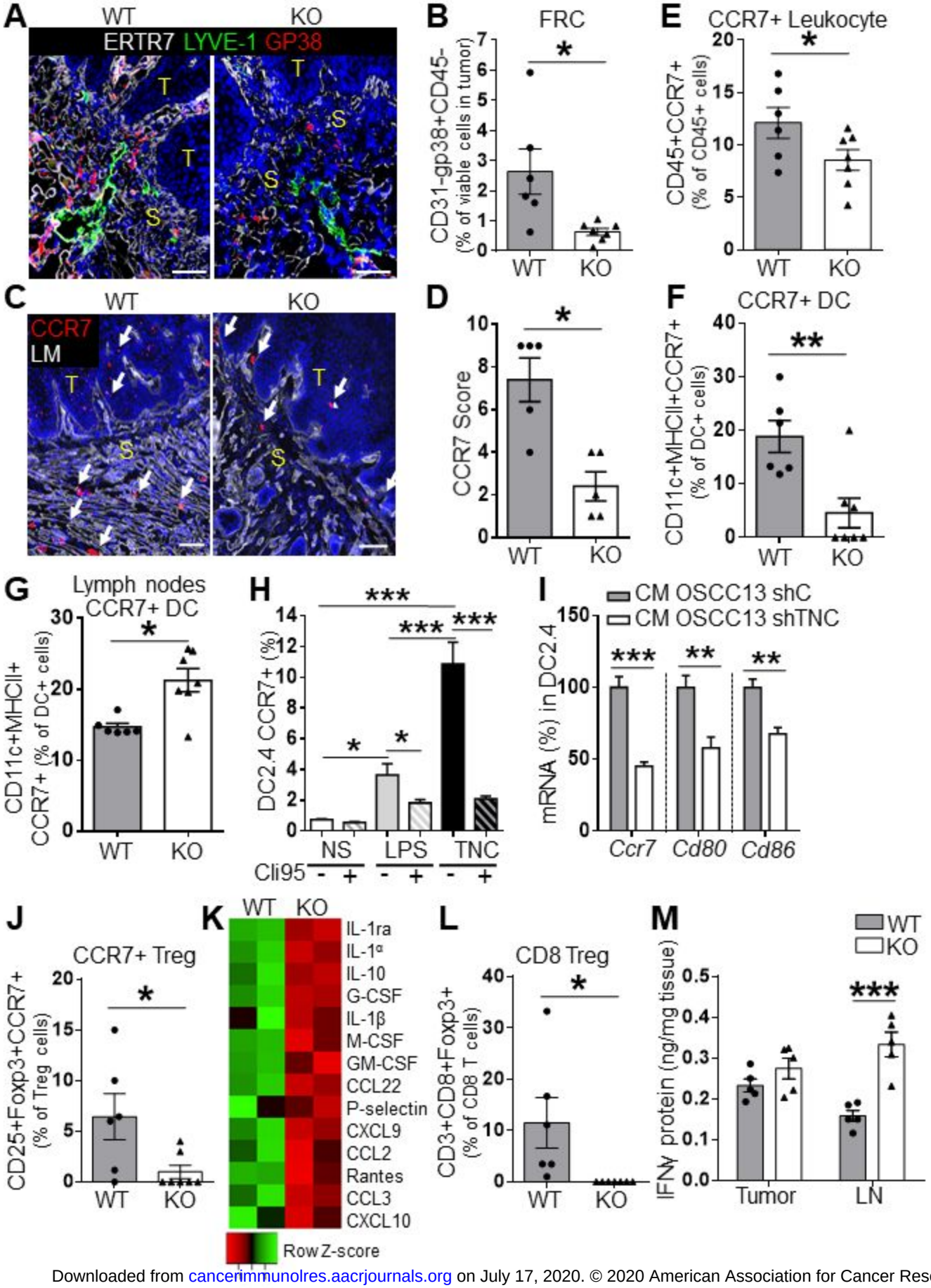

Figure 6

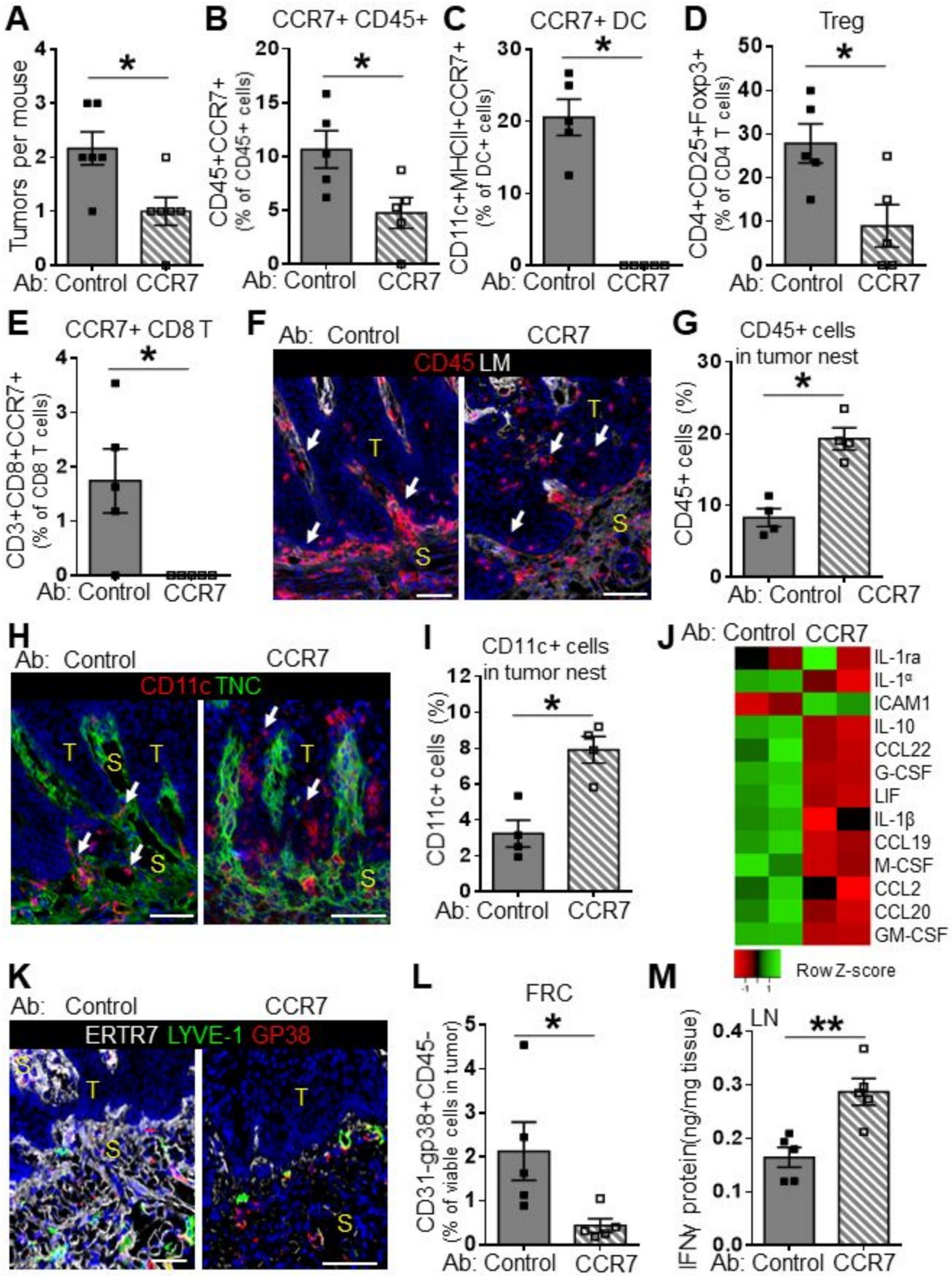

Figure 7

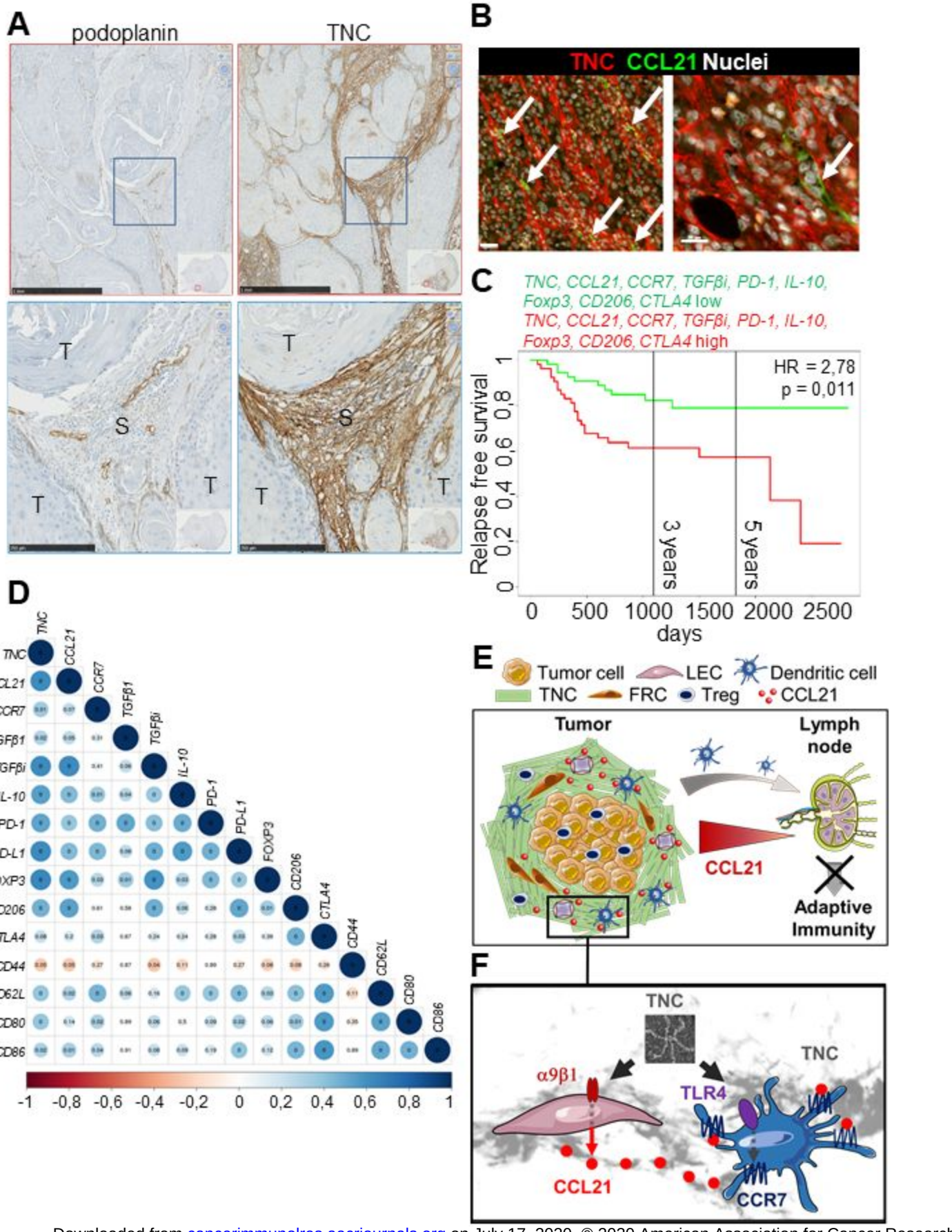

AACR American Association for Cancer Research

Cancer Immunology Research

Tenascin-C orchestrates an immune suppressive tumor microenvironment in oral squamous cell carcinoma

Caroline Spenlé, Thomas Loustau, Devadarssen Murdamoothoo, et al.

Cancer Immunol Res Published OnlineFirst July 14, 2020.